Universität Zürich

Probing the effects of a Mixed Dark Matter scenario using Weak Gravitational Lensing and Cosmic Microwave Background observations

Master thesis for completion of the Master in Science at the University of Zürich

Fabian Hervas Peters

under the supervision of

Prof. Dr. Aurel Schneider

At the Institute for Computational Science

Universität Zürich

Contents

1 Introduction

By the end of the XXth century the ΛCDM model had imposed itself as the standard model of cosmology due to its power to explain the accelerating expansion of the Universe and the observed formation of structure. With this model two physical elements were broadly accepted by the physics community: cold dark matter and Dark Energy. Despite the lack of a consensual explanatory model these entities were adopted for their phenomenological properties. Dark Energy expands space and is therefore responsible for a Universe in accelerated expansion. Cold dark matter is matter which we know interacts gravitationally and participates in the formation of structure while not interacting with particles of the Standard Model in any significant proportion. The "Cold" nature of Dark Matter refers to its mass, or more accurately its velocity. From the structure formation history it seems that a Dark Matter component which was non-relativistic at very-early times and therefore quickly got trapped in gravitational structures provided the best match to observations [Blumenthal et al., 1984].

Once this paradigm was established direct detection experiments and accelerator experiments started looking for a viable dark matter candidate which would be found through a very rare interaction with Standard-Model particles. While these probes are ongoing [Aprile and Aalbers, 2018] [ATLAS, 2021], there are more indirect methods of determining Dark Matter properties. In particular when looking at the gravitational impact of Dark Matter in cosmological and astrophysical observations no interaction with Standard Model particles is necessary.

In addition to the importance of investigating which Dark Matter properties are potentially allowed by its phenomenological effects, a few discrepancies in the ΛCDM structure formation formalism motivate to test scenarios which go beyond the cold dark matter paradigm. One particular problem is the "core-cusp" problem [de Blok, 2010], which is the discrepancy between simulations which predict a very cored halo-profile, with a very steep density profile in the halo-center, while observations tend to prefer a more cuspy profile, which is more flattened-out at small halo-radii. A second long-standing problem is the "missing satellite" problem [Moore et al., 1999] which indicates that ΛCDM simulations predict far more Satellite galaxies than observed in current observations. While more recent observations [Nadler et al., 2021] find more satellite galaxies, the discrepancy remains. These considerations pushed the investigation of a "mixed dark matter" model [Boyarsky et al., 2009] composed of a Cold and a Hot/Warm part. While not necessarily meant to be physically exact, this model tries to work out the impact of a fraction of hot/warm matter on the formation of structure. In particular with enough cold dark matter the predicted down-top structure formation, with gravitational structures starting small and progressively growing, would still be allowed.

A very important probe to investigate the mixed dark matter model (MDM) are observations of the Lyman-α forest [Baur et al., 2017]. These observations look at the 1-D flux power spectrum of Lyman-α photons emitted by distant quasars and then infer the hydrogen density along the line of sight. This allows to probe the matter power spectrum at high redshifts and relatively low-k, meaning small scales, which is where the effects of a mixed dark matter scenario on structure formation differ strongest from the ΛCDM scenario. These Lyman-α observations are difficult due to the many systematic errors such as baryonic effects and uncertainties on the reionization history. While previous bounds for a pure warm dark matter scenario where $m_{TR} > 2.1$ keV and $m_{TR} > 4.65$keV respectively, [Boyarsky et al., 2009] [Baur et al., 2017], recent work taking into account larger uncertainties on the reionization history bring this bound to $m_{TR} \geq 1.5$keV [Garzilli et al., 2021] The TR subscript stands for the *Thermal Relic* mass definition. This results strengthen our motivation to independently probe the MDM scenarios using cosmic shear measurements.

Weak lensing surveys like KiDS, DES and CFHTLens [Heymans et al., 2021], [DES collab. et al., 2019], [Van Waerbeke et al., 2013] imposed themselves as a strong cosmological probe in the past decade

and future surveys like Euclid and LSST [Sartoris et al., 2016] [LSST collab., 2018] will improve these constraints through wider and more precise observations. The prospect of precise upcoming surveys represents a motivation to test constraining MDM scenarios using cosmic shear measurements.
In this work we will use data from the KiDS-1000 survey [Asgari et al., 2021] and the Planck-18 TTTEEE spectra [Planck col. et al., 2020] to constrain a mixed dark matter scenario with $m_{wdm} \in [0.01, 1.5\text{keV}]$.
We will start by quickly reviewing the theoretical aspects of warm/hot dark matter in cosmology and its particle physics motivation. We then briefly present the modelled observations before describing the tools used to produce a prediction. We finally present the constraints obtained on the MDM scenario, before turning our attention to the impact on the S_8 tension.

2 Theory

2.1 The Standard Model of Cosmology

The structure we use to explain the evolution of our universe today was developed in the first decades of the 20th century. It originated with Einstein's formulation of General Relativity, in which space and matter are connected through the Einstein equation:

$$G_{\mu\nu} \equiv R_{\mu\nu} - \frac{1}{2} g_{\mu\nu} = 8\pi G T_{\mu\nu} - \Lambda g_{\mu\nu} \tag{1}$$

with:

- $g_{\mu\nu}$ the metric. This is the central quantity in General relativity which gives the causal-structure of a given space-time
- $R_{\mu\nu}$ and R the Ricci Tensor and Ricci scalar, defined by derivatives of the metric
- $T_{\mu\nu}$ the stress-energy tensor of all matter species in the universe
- Λ the Cosmological Constant

To define the metric of our universe two principles were assumed. The first one is the Copernican principle, meaning that our universe is assumed to be spatially homogeneous. The second assumption is isotropy, meaning that physical conditions are independent of direction.
These assumptions give rise to the Friedman-Robertson-Walker(FRW) metric, defining our universe as:

$$g_{\mu\nu} dx^\mu dx^\nu = -dt^2 + a(t)^2 \left(\frac{dr^2}{1 - kr^2} + r^2 (d\theta^2 + \sin^2 \theta d\phi^2) \right) \tag{2}$$

- t the physical time
- r,θ,ϕ the spatial comoving coordinates which are not sensitive to the dynamics of expansion
- k the spatial curvature, assumed to be 0 throughout this work, meaning the universe is flat
- $a(t)$ the scale factor weighting the distances

The scale factor is a central object of study in Cosmology as it describes the expansion of our Universe. Its evolution is determined from the content of our universe, by inserting the FRW metric

into the Einstein equations. Doing that one gets the description of the evolution of the scale factor given by the first Friedman equation:

$$\left(\frac{\dot{a}}{a}\right)^2 = \frac{8\pi G}{3}\rho + \frac{\Lambda c^2}{3} \tag{3}$$

The energy density ρ scales differently based on the considered component, in particular

$$\rho_{matter} \sim a^{-3} \, , \rho_{radiation} \sim a^{-4} \, , \rho_{vacuum} \sim 1 \tag{4}$$

We define the Hubble parameter $H \equiv \frac{\dot{a}}{a}$ and the normalised densities Ω_i using the critical density $\rho_{crit} = \frac{3H^2}{8\pi G}$. The subscript 0 denotes the quantites at present time. We therefore get the relations:

$$\Omega_i = \frac{\rho_i}{\rho_{crit}} \; ; \quad \sum_i \Omega_i = 1 \; (for \; flat \; universe) \tag{5}$$

And the remodeled Friedman equation:

$$H(a) = H_0(\Omega_r a^{-4} + \Omega_m a^{-3} + \Omega_\Lambda)^{1/2} \tag{6}$$

The dynamics in the early universe are described using a thermodynamical equilibrium. Starting from a very dense and hot state, the universe progressively cools down due to expansion and particles are said to "decouple" ones they do not interact sufficiently with the rest of the particles to stay in equilibrium. The decoupling moment occurs when the interaction rate Γ is of the same order as the Hubble parameter:

$$\Gamma(a_{dec}) \sim H(a_{dec}) \tag{7}$$

with $\Gamma \sim \sigma v n$, where v is the velocity, n the number density and σ the interaction cross section of the particle. Heavier particles will decouple before lighter ones.

2.2 Structure Formation with Hot/Warm thermal relics

In the ΛCDM paradigm, the dark matter contribution is composed of cold matter. The nature of dark matter was debated in the 1980's and 1990's. The terms of hot, warm and cold dark matter were coined to categorize the differences produced on structure formation of these different particles. In the 1990's the cold dark matter was widely accepted due to its explanation of structure formation in a bottom-top way as described in [Blumenthal et al., 1984].
Hot, warm and cold dark matter are distinguished by their thermal velocities v_t at matter-radiation equality. For cold dark matter this velocity is null and it does not prevent the gravitational collapse of matter at any scale. In the hot and warm dark matter scenarios, the particles have a thermal velocity:

$$\langle v_t \rangle = \frac{\langle p \rangle}{m} \sim \frac{3T_\nu}{m_{sterile}} \tag{8}$$

This velocity decreases with the expansion of the Universe and v_t scales with $v_t \sim a^{-1}$. As the hot/warm dark matter particles have a greater velocity, they do not get trapped in a gravitational potential to form bound systems in early times [Schneider, 2012].
The physically relevant parameter is the Jean's length presented in Equ.9. This predicts the length at which pressure forces resist gravitational collapse and we have a system in equilibrium. For smaller wavelength/bigger k's, the gravitational forces are stronger than pressure forces and the perturbations with $\lambda > \lambda_J$ collapse.

$$k_J \equiv k_{fs} = a \sqrt{\frac{4\pi G \rho_m}{\langle v \rangle^2}}\Bigg|_{t=t_{eq}} = 14/\mathrm{Mpc} \left(\frac{m_{wdm}}{0.5\mathrm{keV}}\right)^{4/3} \left(\frac{0.5}{f_{wdm}}\right)^{5/6} \tag{9}$$

The time t_{eq} is the time at matter-radiation equality, where $\Omega_m(z_{eq}) = \Omega_{rad}(z_{eq})$.
The Jeans length therefore gives us the free-streaming length, which is the largest scale at which warm dark matter suppresses the formation of structure. One can define an associated free-streaming mass which gives a threshold value below which Halo formation is suppressed. We write it:

$$M_{fs}(\omega_{wdm}, m_{wdm}) = \left(\frac{\Omega_{wdm}}{0.3}\right)^{1.45} \left(\frac{h}{0.65}\right)^{3.9} \left(\frac{1\mathrm{keV}}{m_w dm}\right) 3.45 M_\odot/h \tag{10}$$

Where $M_\odot$ is the unit of solar mass. This suppression was a strong motivation in the 1990's and 2000's for warm dark matter as it solved the "missing satellite" problem [Moore et al., 1999]: simulations were predicting small companion galaxies to our Milky Way but these were not detected at that time. While some companions have been discovered today [Nadler et al., 2021], the abundance of small-scale clustered matter remains an open question. This point is beautifully shown in N-body simulations, as in Fig.1, where one can see that the abundance of small clusters is stronger in the cold dark matter Scenario, while only the larger structures exist in the MDM and WDM cases.

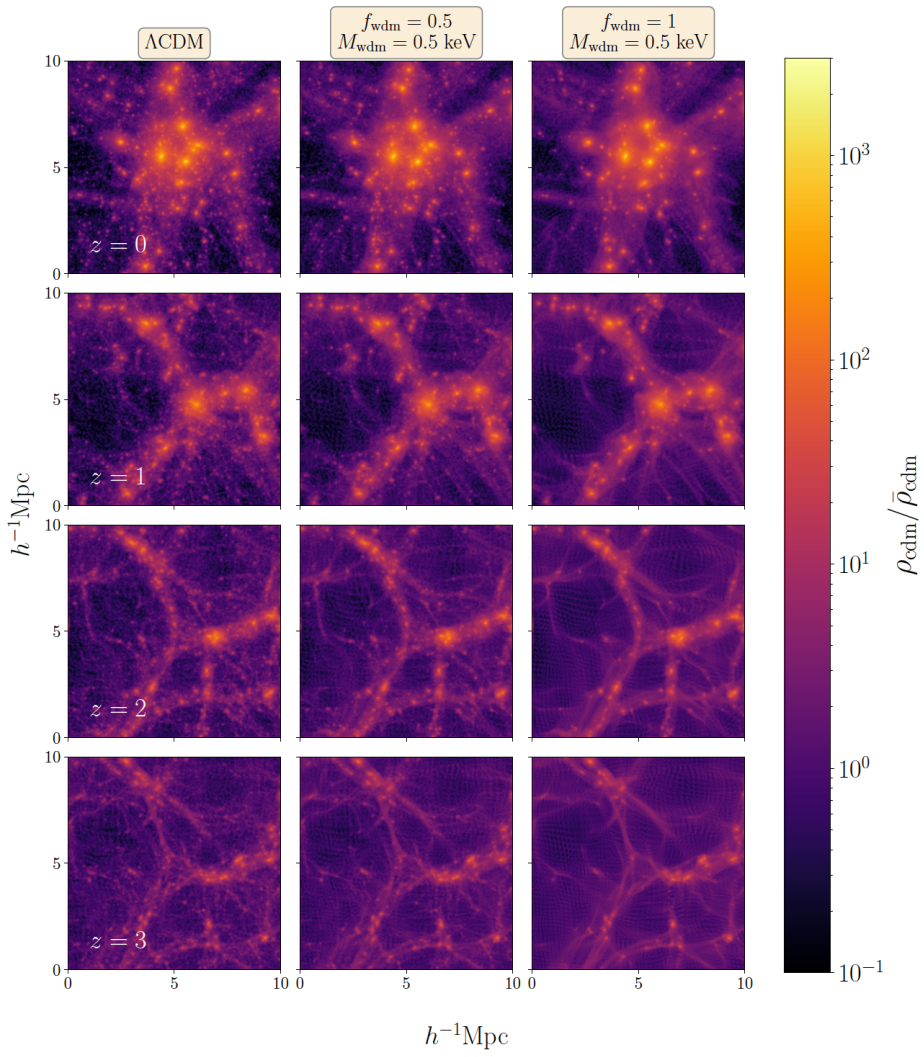

Figure 1: Simulations of a cold dark matter, mixed dark matter and warm dark matter Universe respectively. One can see going from left to right that the structure gets smoothed out and only the bigger structure remains due to suppression from the thermal velocities, source: [Parimbelli et al., 2021]

2.3 The S_8 Tension

Towards the end of the XXth century, multiple ways of probing the cosmological scenario were developed. While ΛCDM eventually imposed itself as the most explicative theory, the precision reached by observations today allow to probe if the measured values of the cosmological parameters agree between very high and low redshift.
While the tension on the Hubble rate H_0 has gained a lot of attention recently [Abdalla and Abellán, 2022], another tension which has come under scrutiny is the S_8 tension, a parameter defined as:

$$S_8 = \sigma_8 \sqrt{\frac{\Omega_m}{0.3}} \tag{11}$$

The quantity σ_8 is the parameter σ defined in Equ.21, evaluated on a radius of $r = 8h/\text{Mpc}$. It measures the amount of clustering of matter on $8h/\text{Mpc}$ spheres predicted from the linear theory.

This parameterization of S_8 was introduced to break the degeneracy between σ_8 and Ω_m. The degeneracy is caused by the incapability of weak lensing measurements to distinguish between a very clumpy Universe which has little matter density and a very smeared out universe which has a very high matter density, as both these scenarios would produce the same lensing potential. In Fig.2 one can see the discrepancy between measurements of high redshift probes at the top of the plot and all the low redshift probes at the bottom. A clear trends appears for very diverse types of probes.

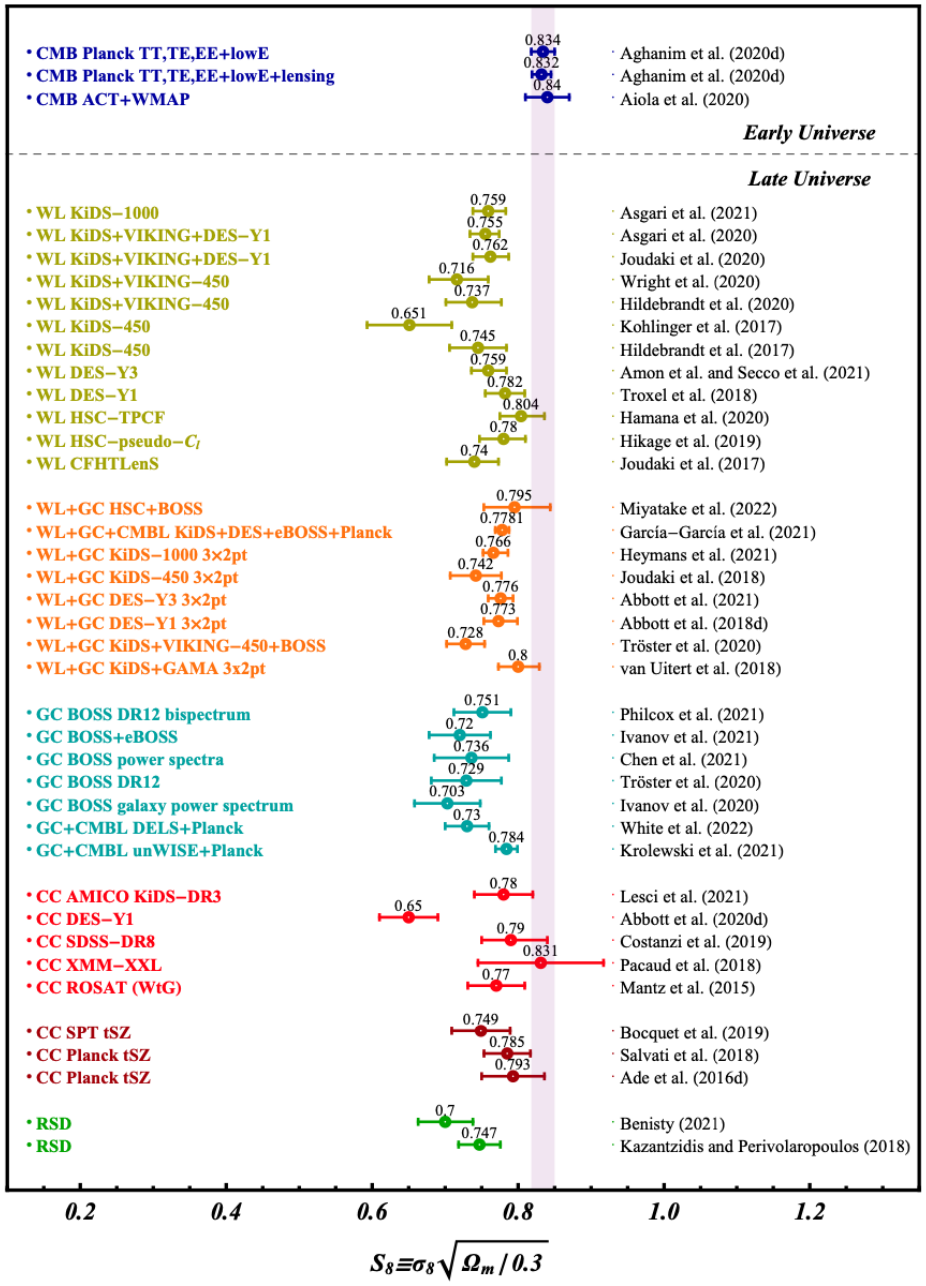

Figure 2: The values of $S8$ for the probes: WL-Weak Lensing, GC-Galaxy Clustering, CMBL-CMB Lensing, CC-Cosmic Chronometer, RSD- Redshift Space Distortions, source: [Abdalla and Abellán, 2022]

2.4 Weak Lensing Theory

Since Einstein established his theory of relativity, we know that massive objects bend the space-time surrounding them and therefore light does not go in "straight" lines but follows geodesics that can be warped in the vicinity of heavy object. Different lensing phenomena are classified as strong, micro and weak-lensing. The strong-lensing case is the most telling and the best illustration of the

process. Strong-lensing occurs when light from a far placed background object gets distorted by a massive foreground object placed on its path. The resulting bending of space acts exactly as a lens, bringing light-rays to the observer which would otherwise have never reached him. The most elegant illustration of this phenomena are Einstein-rings, shown in Fig.3, where the perfect alignment of a background source and a foreground lens create a ring the observer on earth can see.

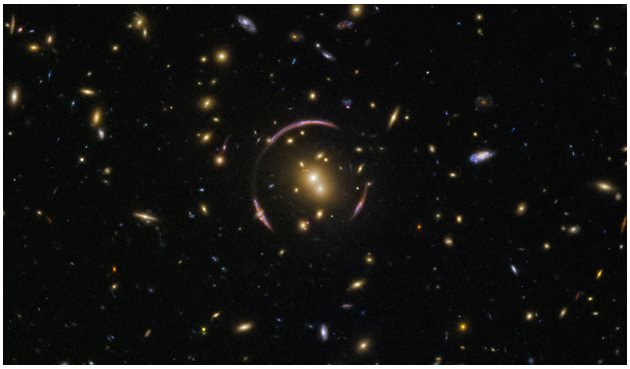

Figure 3: Einstein-ring from a red-galaxy capture by the Hubble telescope, source:NASA

While less photogenic, weak lensing measurements have gained a lot of attention in recent years as a cosmological test. In this case, the background sources are always galaxies and the lens is the matter placed between the source and the observer. As we know that dark matter interacts gravitationally, it will act as a lens if placed in proximity of the path of the light, distorting the shape of the galaxy. This offers the interesting prospect of producing a dark matter distribution map on the sky.
In this section we want to review the Cosmic Shear theory presented in [Bartelmann and Schneider, 2001], as it forms the basis of our modeling pipeline.

In Fig.4 one can see β being the direct angle to the observed system, and Θ the observed angle which takes into account the deflection by the lens. The distortion of the light is quantified by the Jacobian matrix:

$$\mathcal{A} = \frac{\partial \beta}{\partial \theta} = (\delta_{ij} - \frac{\partial^2 \psi(\theta)}{\partial \theta_i \partial \theta_j}) = \begin{pmatrix} 1-\kappa-\gamma_1 & -\gamma_2 \\ -\gamma_2 & 1-\kappa+\gamma_1 \end{pmatrix} \tag{12}$$

with:

- ψ the deflection potential
- κ the dimensionless surface mass density
- γ the shear with $\gamma \equiv \gamma_1 + i\gamma_2$

The deflection potential obeys the Poisson equation in two dimensions

$$\nabla^2 \psi = 2\kappa \tag{13}$$

The shear is the observable quantity, it is decomposed into a tangential and a cross-component as: $\gamma_t = -\Re[\gamma e^{-2i\varphi}]$ and $\gamma_x = -\Im[\gamma e^{-2i\varphi}]$. In the weak lensing regime the shear can be understood as the elliptical deformation of the image, as shown in Fig.5. The tangential and cross-components are the decomposition of the shear relative to the distortion angle φ.

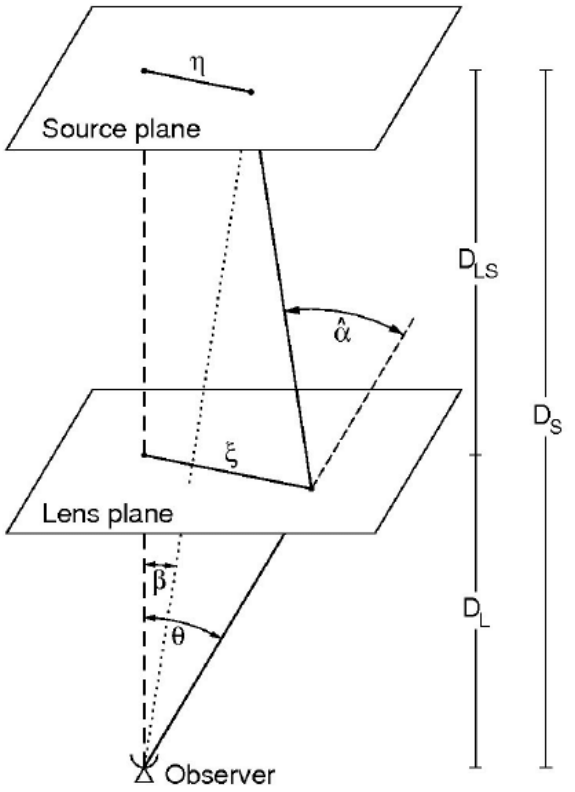

Figure 4: Image distortion of a gravitational Lens, source: [Bartelmann and Schneider, 2001]

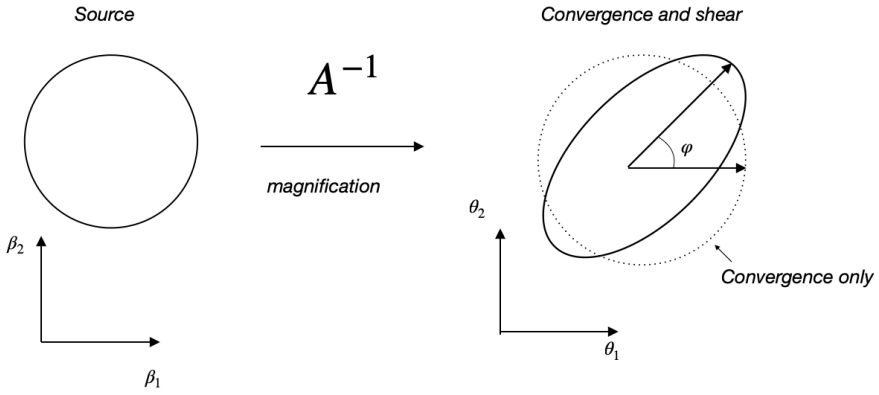

Figure 5: Distortion of an image in direction φ

The shear produced by the deformation of the light path can not be measured for a single galaxy as the true galaxy shape is unknown. Instead it is assumed that over a very large number of galaxies the intrinsic orientations are randomly aligned and that the galaxies close to each other can present a coherent deformation as their light is lensed by the same structure. This can be quantified by the correlation functions defined as:

$$\xi_{\pm} = \langle \gamma_t \gamma_t \rangle(\theta) \pm \langle \gamma_x \gamma_x \rangle(\theta) \tag{14}$$

where θ is called the separation vector and represents the angle between two galaxies.
Now that we have some understanding of the observable quantity, we need to understand how it can be used as a cosmological probe.

In the cosmological theory, a key prediction is the evolution of the inhomogeneities in time. These are quantified by the power spectrum $P(k)$ defined as:

$$\langle\tilde{\delta}(\vec{k})\tilde{\delta}(\vec{k'})\rangle = (2\pi)^3 P(k)\delta^3(\vec{k}-\vec{k'}) \tag{15}$$

where $\delta(\vec{x})$ gives the deviation of the field from a mean in position space, and $\tilde{\delta}(\vec{k})$ is the Fourier transform of that deviation. The power spectrum has been measured by a variety of probes at different scales which are presented in fig6.

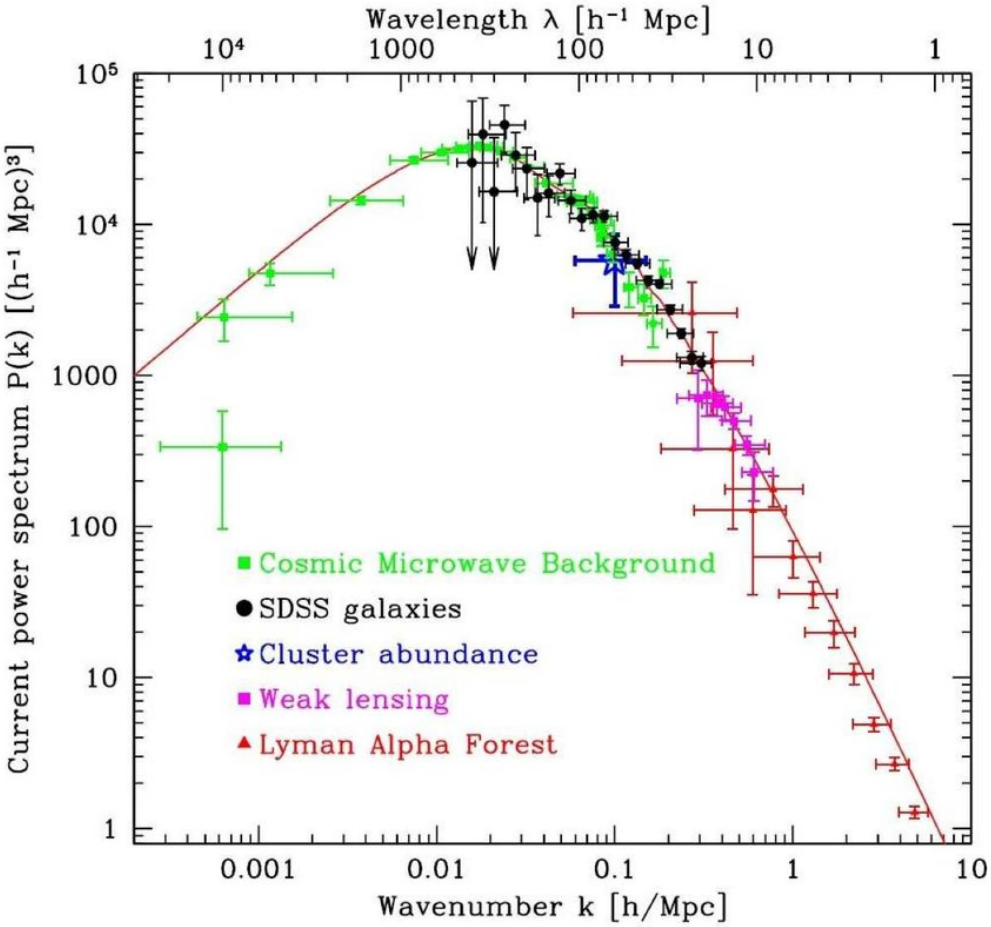

Figure 6: The matter power spectrum measured by different methods, source: [Niemi, 2011]

In a weak lensing photometric survey, the goal is to measure the shape of a large number of galaxies, in the order of millions, with only an approximate information on their distance. The challenge is then to measure an initially 3-dimensional quantity (the power spectrum), using limited information on the distance along the line-of-sight.
We consider two bent light rays that reach an observer as presented in Fig.7. From the lensing formalism we get a *lensing potential* ϕ, related to the newtonian potential Φ via:

$$\psi(\Theta, w) = \frac{2}{c^2} \int_0^{\chi} d\chi' \frac{f_\kappa(\chi - \chi') f_\kappa(\chi')}{f_\kappa(\chi)} \frac{\partial^2}{\partial x_i \partial x_j} \Phi(f_\kappa(\chi')\Theta, \chi') \tag{16}$$

Here f_κ represents the comoving angular diameter distance. This allows to express the Jacobi matrix from the lensing diformation as: $A_{ij} = \delta_{ij} - \partial_i \partial_j \psi$

The surface density κ is related to the lensing potential via $\kappa = \nabla^2 \psi / 2$ and for a matter distribution

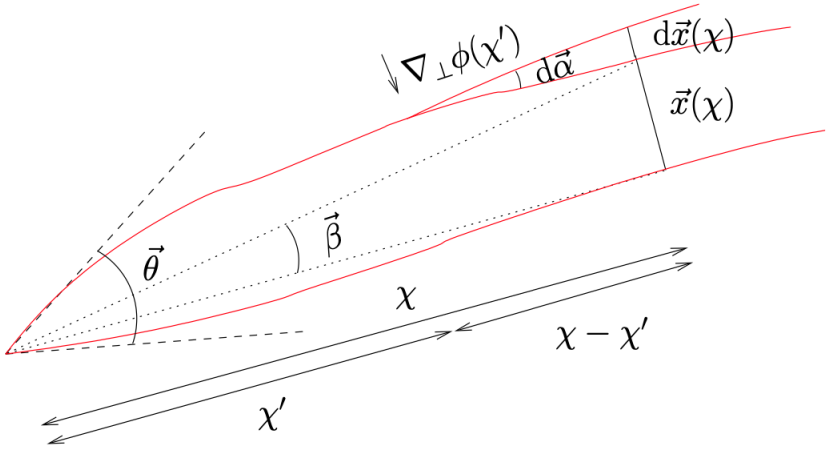

Figure 7: Two light rays originating at distance χ with a lens at χ', ϕ is a Bardeen gravitational potential, source: [Kilbinger, 2015]

along the line of sight we can find:

$$\kappa(\Theta) = \frac{2H_0^2 \Omega_m}{2c^2} \int_0^{\chi_{lim}} \frac{d\chi}{a(\chi)} q(\chi) f_\kappa(\chi) \delta(f_\kappa(\chi)\Theta, \chi) \tag{17}$$

where $q(\chi)$ is the lens efficiency. The cosmological quantities Ω_m, H_0, a and δ therefore play a role here due to the 3-D Poisson equation of the newtonian gravitational potential Φ in comoving coordinates:

$$\nabla^2 \Phi = \frac{3H_0^2 \Omega_m}{2a} \delta \tag{18}$$

We can use the Fourier transform of the correlation to obtain the convergence power spectrum P_κ, which is the central quantity in cosmic shear measurements. The variable giving the separation of the correlation is the multipole moment ℓ approximately given by $\ell \sim 2\pi/\theta$ with θ the separation angle in the sky. The Fourier transform therefore is:

$$\langle \tilde{\kappa}(\ell) \tilde{\kappa}^*(\ell') \rangle = (2\pi)^2 \delta_D(\ell - \ell') P_\kappa(\ell) \tag{19}$$

The 2-dimensionsal convergence power spectrum can finally be related to the 3-dimensional matter power spectrum via the Limber equation, using particular weight functions $g_i(\Theta) = \int d\chi q_i(\chi) \delta(f_\kappa(\chi)\Theta, \chi)$. This weighting comes from [Limber, 1953] where it was used to compute the distribution of extra-galactic nebulae. It encodes the fact that the 2D projection of a 3D random field (projection along the line of sight) still represents the realization of an isotropic random field.
Therefore the convergence power spectra can be expressed as:

$$P_\kappa(\ell) = \frac{9H_0^4 \Omega_m^2}{4c^4} \int_0^{\chi_{lim}} d_\chi \frac{g^2(\chi)}{a^2(\chi)} P_\delta(k = \frac{\ell}{f_\kappa(\chi)}, \chi) \tag{20}$$

While one could believe that this quantity is sensitive to H_0, due to the power 4, a change in H_0 would only rescale the angular diameter distance and the mass density, which would have little impact on the shear correlation functions, for a detailed discussion see [Hall, 2021].
While cosmic shear is not sensitive to H_0 it is particularly sensitive to $\Omega_{m,0}$ and to the clumpiness of matter represented by the parameter σ_8: the variance of the density contrast field over a radius of 8Mpc. This parameter gives the integral of the linear power spectrum with a top hat-function $W(kR)$ in Fourier space.

$$\sigma^2(R) = \int_0^\infty \frac{dk}{k} \frac{k^3 P(k)}{2\pi^2} |W(kR)|^2 \tag{21}$$

where the value of $R = 8\text{Mpc}/h$ has been historically chosen for σ_8 to be close to unity. As the integration runs over all k's it is often seen as a normalization of the matter power spectrum at present time. For a given cosmological scenario there is a direct mapping with another parameter A_s that we will introduce in Sec.3.2, but we can already note that the correspondence between A_s and σ_8 depends on the considered cosmological scenario as the first one gives the normalization at initial time, while the latter gives the normalization today.
Cosmic shear measurements can be modeled from the Non-linear matter power spectrum using the Limber approximation, which will be the main objective of our modeling pipeline.

2.5 A right handed neutrino in the Electro-Weak Standard Model of Particle Physics

For the hot/warm component of our mixed dark matter model, our preferred candidate is the Dodelson-Widrow (DW) sterile neutrino, presented in [Dodelson and Widrow, 1994]. The DW neutrino is a right-handed sterile neutrino. It therefore forms a natural extension of the Standard Model of particle physics. In the Electro-Weak Standard Model of particle physics, the left-handed neutrino is massless, which we know to be incorrect from oscillation experiments [Fisher et al., 1999]. In the Standard Model the lepton masses are produced by Yukawa coupling with the Higgs Field. The necessity to produce masses via Yukawa coupling is due to the fact that a Majorana or Dirac mass term would break $SU(2)$ gauge invariance for a particle which is an $SU(2)$ doublet, such as the left handed leptons. The Lagrangian term of the Yukawa coupling is given by:

$$\mathcal{L}_{Yuk} = -\frac{v+\eta}{\sqrt{2}} \sum_{i=1} 3 m_{l,i} (\bar{l}^i_L l^i_r + h.c.) \tag{22}$$

where the Higgs doublet is expanded around its vacuum expectation value v and expressed in the unitary gauge:

$$\phi = \frac{1}{\sqrt{2}} \begin{pmatrix} 0 \\ v+\eta \end{pmatrix} \tag{23}$$

and $m_{l,i}$ is the mass of the lepton flavor i and is expressed $m_{l,i} = \frac{\lambda^l_i v}{\sqrt{2}}$
The right-handed neutrino is not an anomaly in the Standard model, it is simply sterile which means it has 0 quantum number in all gauge groups:

	ν_l	e_l	ν_r	e_r
I^3	$\frac{1}{2}$	$-\frac{1}{2}$	0	0
Q	0	-1	0	-1
Y	-1	-1	0	-2

Table 1: Quantum Numbers for the Electro-Weak Standard Model

With the quantum numbers:

- I^3 the third component of the Isospin I, which gives the transformation in the gauge group $SU(2)_L$
- Y the hypercharge which gives the transformation in the gauge group $U(1)_Y$
- Q which is not a quantum number of the standard model, but the conventional electric charge expressed $Q = I_3 + Y/2$, which gives the transformation for $U(1)_{E.M.}$

2.6 Sterile neutrinos in cosmology

From Tab.1 it is clear that the right-handed neutrino is sterile under $SU(2)_L \times U(1)_Y$ transformations and a Majorana mass term for ν_r will therefore not break any gauge invariance.
This lead Dodelson Widrow to propose for their sterile neutrino candidate:

$$\mathcal{L} = \mu \left(\frac{\phi}{v}\right) \bar{\nu}_L \nu_R + M \nu_r \nu_r + h.c \tag{24}$$

In this Lagrangian only one generation of leptons is considered for simplicity, μ is the Yukawa mass of the left-handed neutrino called *active neutrino* and the right-handed neutrino called *sterile neutrino* who has both the Yukawa mass μ and a Dirac mass M. In the seesaw model $M \gg \mu$.
At tree level, the right-handed neutrino is produced through mixing with the active neutrino, the Boltzmann equation for the sterile neutrino is:

$$\left(\frac{\partial}{\partial t} - HE\frac{\partial}{\partial E}\right) f_s(E,t) = \left(\frac{1}{2}\sin^2[2\theta_m(E,t)]\Gamma(E,t)\right) f_A(E,t) \tag{25}$$

The parameter $\sin^2(2\theta_m)$ is the mixing angle between active and sterile neutrinos. Here f_s and f_a represent the distribution functions of the active and sterile neutrino. This is a very important quantity as one can infer the density of a species i through:

$$n_i = 2\int d^3p \frac{f_i}{2\pi^2} \tag{26}$$

In previous efforts, a normal assumption was that the sterile neutrino would constitute the totality of dark matter. As this scenario is not favored by observations due to the way structure seems to be forming in accordance with the cold dark matter scenario, it is interesting to investigate if a fraction of dark matter is warm/hot.
From Fig.8 one can see that the entirety of the parameter space has been excluded by astrophysical observations. We are therefore probing the grey band below where $\Omega_{sn} < \Omega_{DM}$ but at masses smaller than those probed in this parameter space.

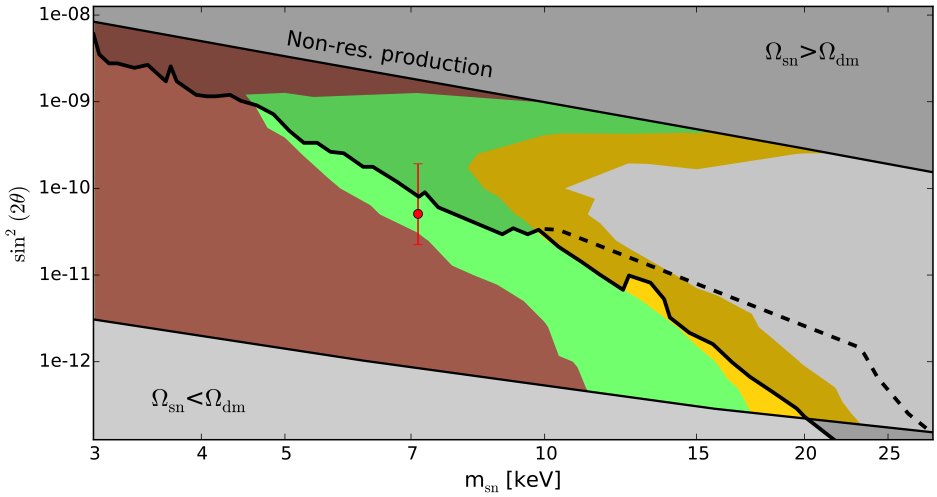

Figure 8: Exclusion plot for sterile neutrino from [Schneider, 2016]: The brown exclusion zone comes from Milky-Way satellite counts, the green and yellow zones are excluded by Lyman α observation, the shaded region comes from X-ray constraints. The red line indicates a signal coming from a 7.1keV unidentified spectral line of galaxy clusters

The considered warm/hot dark matter candidate which makes up a fraction of the dark matter is characterized by its impact on structure formation. As explained in [Acero and Lesgourgues, 2009], there are multiple proposed hot dark matter models that present degenerate cosmological signatures. The equivalent models can be mapped to one another through their impact on the 3 parameters $[\Delta N_{eff}, \omega_s, \langle v_s \rangle]$. We will first present these parameters in detail, then the values for our main candidate the Dodelson-Widrow sterile neutrino and finally see conversions to the other equivalent models.

N_{eff}:The effective number of neutrino species N_{eff} is a parameterization dating back to the 1980's where it was unclear from accelerator physics how many neutrino species existed. Today the number of neutrino species is well established to be 3 $(\nu_e, \nu\mu, \nu\tau)$. Therefore N_{eff} quantifies the relativistic effective degrees of freedom populating the universe:

$$\rho_R = \rho_\gamma \left(1 + \frac{7}{8}\left(\frac{4}{11}\right)^{4/3} N_{eff}\right) \tag{27}$$

The factor $\frac{4}{11}$ comes from the neutrinos decoupling before photons, which stay in equilibrium longer due to there interactions with the protons and electrons. The number N_{eff} coming from neutrinos has been quite precisely calculated to be 3.0440 ± 0.0002 according to [Bennett et al., 2021]. The small deviation from 3 comes from the fact that decoupling is not instantaneous. The measurement of N_{eff} today is quite restrictive, with [Planck col. et al., 2020] measuring: $N_{eff} = 2.99 \pm 0.17$. For a comparison of results between different likelihoods see: [Henrot-Versillé et al., 2019]. With this rather stringent bounds it is quite clear that from cosmological considerations, a fourth neutrino in a mass range similar to its 3 cousins is discarded, as its contribution to N_{eff} would be too large. Nevertheless a lot of particle physics predictions which go beyond the standard model would contribute to N_{eff}, as for example the QCD axion, the QCD Majoron or light fermions. Recently, measurements of N_{eff} have come under scrutiny as they could help to alleviate the Hubble tension as done in [Nunes and Bonilla, 2018], who combine CMB and Large scale structure measurements which

indicate a departure from N_{eff} given as $\Delta N_{eff} = 0.614 \pm 0.26$. Any supplementary source of radiation at electron-positron annihilation would produce a contribution $\Delta N_{eff} = N_{eff} - N_{eff,SMneutrino}$.

Our sterile neutrino candidate with a phase-space distribution $f(p)$ contributes a supplementary source of dark radiation :

$$\Delta N_{eff} = \frac{\rho_s^{rel}}{\rho_\nu} = \frac{\frac{1}{\pi^2}\int dp\ p^3 f(p)}{\frac{7}{8}\frac{\pi^2}{15} T_\nu^i d^4} \tag{28}$$

The contribution of our sterile Neutrino to ΔN_{eff} in our probed parameter space is shown in Fig.10. The id superscript on T_ν stands for the instantaneous decoupling limit, which is a reasonable approximation to take.
The phase space distribution is an important thermodynamical quantity representing how the momenta of the particles are distributed. For a fermion in equilibrium, or equivalently a thermalized fermion, the phase space distribution is a Fermi-Dirac distribution.

$$f(p) = \frac{1}{e^{(\epsilon_i - \mu)/T} + 1} \tag{29}$$

with ϵ_i the energy of a particle and μ the chemical potential.
ω_s: the current energy density of the additional massive free-streaming particle ω_s can be related to the phase space distribution: .

$$\omega_s = \Omega_s h^2 = \left(\frac{m}{\pi^2}\int dp\ p^2 f(p)\right)\frac{h^2}{\rho_c^0} \tag{30}$$

With ρ_c^0 the critical density today. It is interesting that there is a dependence between ω_s and m which is not necessarily surprising, as the heavier our additional massive particle is, the greater its energy density will be. Furthermore, while here we consider the energy density at present times, which should be constant in time up to background evolution, in more complex models with interactions the respective energy densities can change with time.
$\langle v_s \rangle$: finally the parameter$\langle v_s \rangle$ which is particularly linked to structure formation, is the average velocity of the particles today. The quantity is related to the free-streaming length presented in Equ.9 and indicates the scale at which structure formation (quantified by the power spectrum) is suppressed.

$$\langle v_s \rangle = \frac{\int p^2 dp \frac{p}{m} f(p)}{\int p^2 dp\ f(p)} = \frac{7}{8}\frac{\pi^2}{15}\left(\frac{4}{11}\right)^{4/3}\frac{T_{CMB}^4 h^2}{\rho_c}\frac{\Delta N_e ff}{\omega_s} = 5.618 \times 10^{-6}\frac{\Delta N_{eff}}{\omega_s} \tag{31}$$

From this equation it is clear that the 3 physical parameters only give rise to two degrees of freedom, which in our model are captured by $[m_{wdm}, f_{wdm}]$.

In our parameterization, the phase-space distribution of our sterile neutrino is scaled with χ to give the correct energy density, we therefore have:

$$f(p) = \frac{\chi}{e^{p/T_\nu} + 1} \tag{32}$$

Which means the temperature of our sterile neutrino follows the temperature of the active neutrino.
For the three parameters which dictate the behavior of our model according to [Acero and Lesgourgues, 2009]:

$$\Delta N_{eff} = \chi\omega_s = \frac{m_s}{94.05eV}\chi\langle v_s \rangle = \frac{0.5283meV}{m_s} \tag{33}$$

While we used this sterile neutrino mass in our calculation of the linear power spectrum, we had to convert from the thermal mass for the use of the non-linear emulator and the comparison to other works. To convert we use the formula in equation (6) of [Schneider, 2012] :

$$m(\nu_s) = 3.90\text{keV}\left(\frac{m_{thermal}}{1\text{keV}}\right)^{1.294}\left(\frac{f_{wdm}\Omega_{DM}h^2}{0.1225}\right)^{-1/3} \tag{34}$$

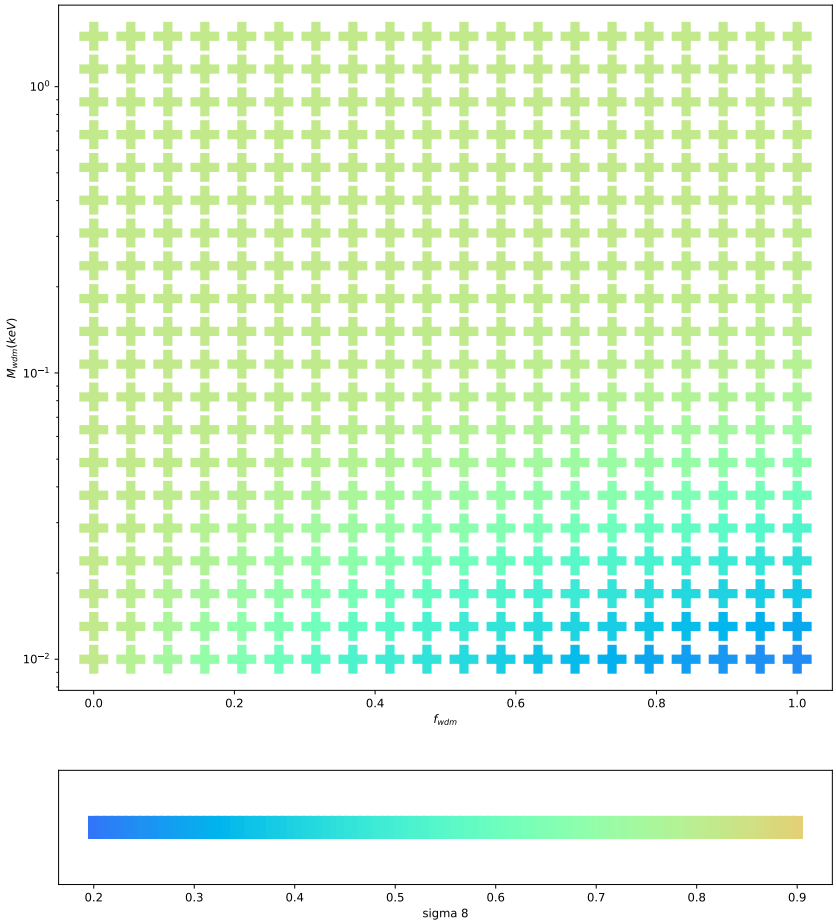

Figure 9: The modification in σ_8 in the selected mixed dark matter parameter space

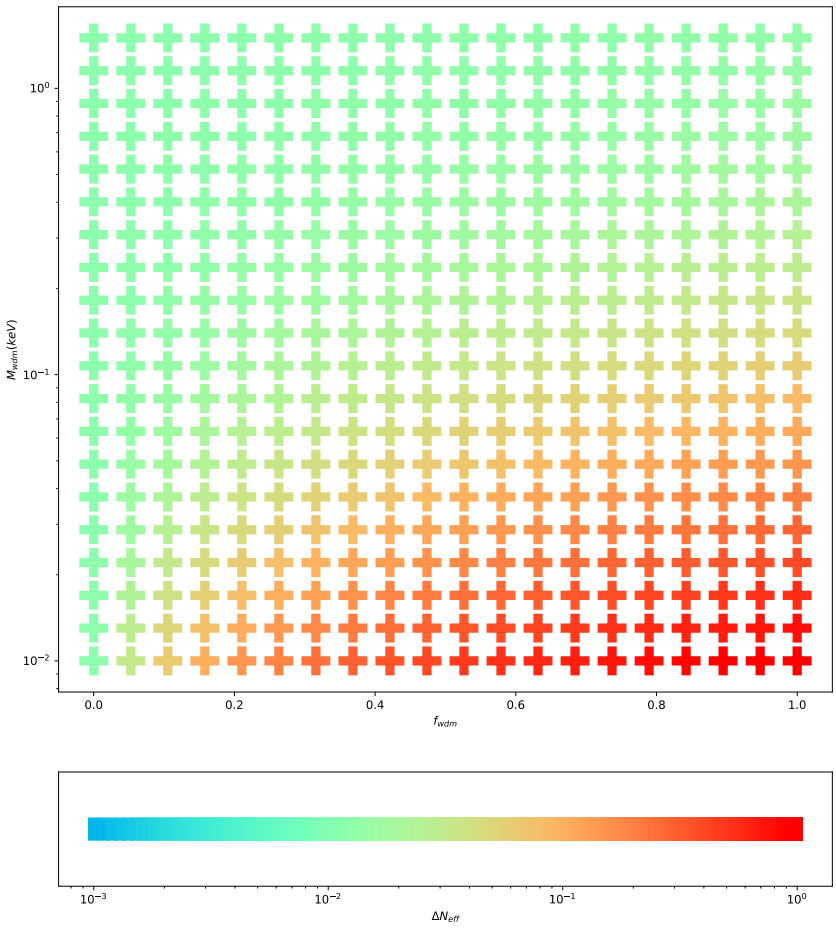

Figure 10: The modification ΔN_{eff} in the selected mixed dark matter parameter space

2.7 Equivalent parameterization

In the thermal mass picture the temperature of the sterile particle decouples from that of the active particle $T_\nu^{act} \neq T_{sterile}$. The particle distribution function is therefore:

$$f(p) = \frac{1}{e^{p/T_s} + 1} \tag{35}$$

And the previously described phenomenological parameters in the Thermal mass case are:

$$\Delta N_{eff} = \left(\frac{T_{sterile}}{T_\nu^{act}}\right)^4 \; ; \; \omega_s = \frac{m_s}{94.05eV}\left(\frac{T_{sterile}}{T_\nu^{act}}\right)^3 \; ; \; \langle v_s \rangle = \frac{0.5283meV}{m_s}\left(\frac{T_{sterile}}{T_\nu^{act}}\right) \tag{36}$$

The two parametrizations we presented are both fully thermalized and follow Fermi-Dirac particle distribution functions. Non-thermally produced species can present very similar phenomenological

signatures as shown in [Bhattacharya et al., 2021].

3 Observations

3.1 The Kilo Degree Survey

We use the gold sample of weak lensing and photometric redshift measurements from the fourth data release of the Kilo-Degree Survey ([Kuijken et al., 2019], [Wright et al., 2020] , [Hildebrandt et al., 2020], [Giblin et al., 2021]), hereafter referred to as KiDS-1000. Cosmological parameter constraints from KiDS-1000 have been presented in [Asgari et al., 2021] (cosmic shear), [Heymans et al., 2021] (3x2pt) and [Tröster et al., 2021] (beyond ΛCDM), with the methodology presented in [Joachimi et al., 2021].
The Kilo Degree Survey is, as its name suggests, a photometric survey of 1000-degrees, therefore covering 1/42th of the sky, recorded in the southern hemisphere using the Very Large Telescope. The data gathering took place from 2011 to 2019. The survey's goal was to produce images of galaxies using 4 successive color filters: ultraviolet, green, red, infrared (u, g, r, i). The goal of the color filters is to give an estimate of the distance at which the galaxies are located by getting the spectrum of each galaxy and assigning a distance based on how the galaxy's spectrum seems redshifted. The golden standard for distance estimation is the use of spectrometry where absorptions lines of different elements allow a precise determination of the redshift, but these require more precise observations which take more time to make in a wide-sky survey. Spectroscopic surveys are used by the KiDS team in the case of overlapping sky-coverage for calibration purposes.

Fig.11 gives a representation of the sky coverage with the VLT in the foreground. The colors in the map represent the dark matter density as inferred from the cosmic shear signal.
The KiDS-survey is shallower then other surveys like the CFHTLens or UNIONS, with ranges in redshift $z \in [0.1; 1.25]$, but it covers a wider portion of the sky while having high resolution allowing to accurately determine the galaxy shapes. The redshift distribution of the KiDS survey is presented in Fig.28. To model the KiDS-1000 data we follow the methodology laid out in [Asgari et al., 2021]. We present our exact methodology in section 4.1
Our goal is to model the angular power spectra $C(\ell)$ and compare it to the data published in the mentioned paper. This allows us to estimate a log-likelihood:

$$\mathcal{L}(\theta_{theo}|p) = -\frac{1}{2}((\theta_{theo} - \theta_{data})^T \text{ Cov }^{-1}(\theta_{theo} - \theta_{data})) \tag{37}$$

with θ_{theo} our prediction vector and p the priors.

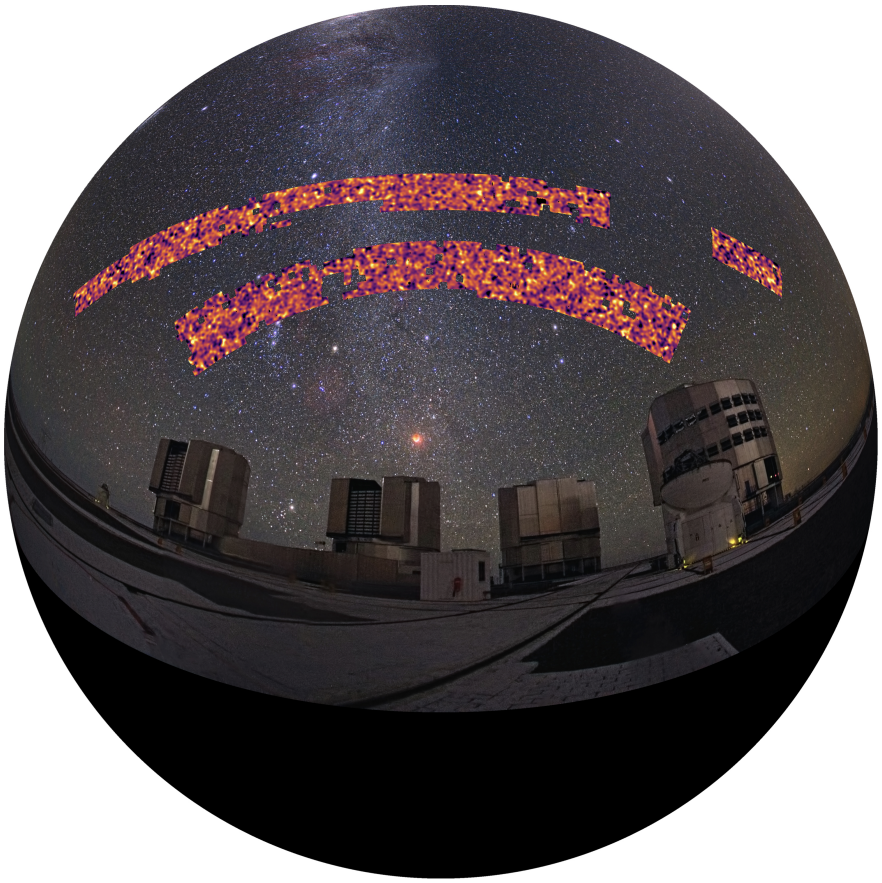

Figure 11: The dark matter map produced by KiDS in the night sky, source:KiDS

3.2 The Cosmic Microwave Background

As the evolution of the universe was debated between a static state and one in expansion, the cosmic microwave background provided the most conclusive evidence for the Big-Bang theory. Up to this day it remains our most precise observation to constrain cosmological scenarios. The physical principle is as follows: while the Universe was in a hot and dense state, space was opaque to photons. This means that photons could not travel very far before colliding into atoms or electrons and being absorbed and reemited. After 300 000 years, the Universe had cooled down enough due to its expansion to become transparent and the photons which were initially trapped in the primordial "soup" suddenly started free-streaming. The photons reach us form all directions of the sky indicating that the whole universe shared a single initial state. The photons one detects in a Cosmic Microwave Background measurement have therefore been travelling to us for 14 billion years. The temperature spectrum they produce is a black-body with a temperature $T_{CMB} = 2.72548 \pm 0.00057K$ [Fixsen, 2009].
Beyond the homogeneous Black-body spectrum, the cosmological information is encoded in the anisotropies of the temperature and polarisation map, the temperature map (which is a 2D projection of the whole sky) is presented in Fig.12. The departure from T_{CMB} are of the order 10^{-4} and yet they are very rich in cosmological information.

For our cosmological prediction we model the temperature anisotropies $\Theta_\gamma = \delta T/\bar{T}$ which follow a

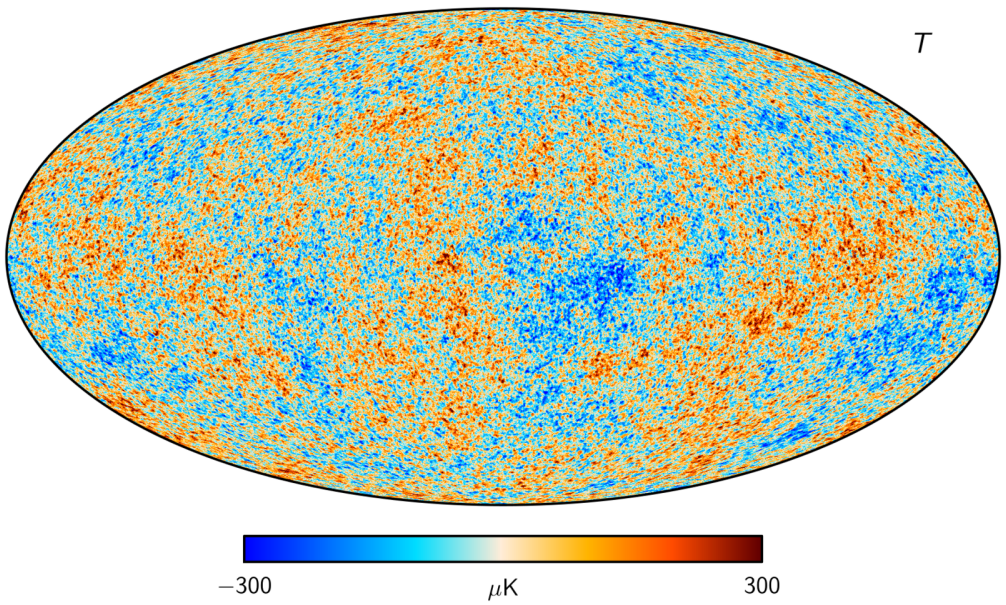

Figure 12: The CMB map of temperature anisotropies, source: Planck collaboration

set of Boltzmann equations. The correlation of the temperature can form a spectrum:

$$\langle \Theta_{\gamma\ell}((\eta, \vec{k})\Theta^*_{\gamma l}((\eta, \vec{k'})\rangle = \frac{2\pi^2}{k^3}\mathcal{P}_{\mathcal{R}}(k)[\Theta_{\gamma\ell}((\eta, k)]^2\delta^3(\vec{k} - \vec{k'}) \tag{38}$$

Where η stands for a conformal time and the initial power spectrum is:

$$\mathcal{P}_{\mathcal{R}}(k) = A_s(k/k_0)^{n_s - 1} \tag{39}$$

The constant k_0 is the pivot scale, A_s is the primordial amplitude and n_s the initial tilt. The two last parameters are free parameters in our analysis while k_0 is fixed.
The observed $C(\ell)$'s are produced by decomposing the sky map of temperature into spherical harmonics. The modeling of the angular correlation function is then:

$$C(\ell) = \frac{1}{2\pi^2}\int \frac{dk}{k}[\Theta_{\gamma\ell}(\eta_0, k)]^2\mathcal{P}_{\mathcal{R}}(k) \tag{40}$$

To obtain the predictions we use the CLASS module presented in [Lesgourgues and Tram, 2011a] and [Lesgourgues and Tram, 2011b] and retrieve the lensed $C^{TT}(\ell), C^{TE}(\ell), C^{EE}(\ell)$ where E indicates the E-polarization of the photons and TE is the Temperature-E-polarization cross-correlation. The effect on the linear theory of a warm dark matter species is described in [Ma and Bertschinger, 1995]. One parameter which we require in our analysis is the optical depth τ. The optical depth comes from free electrons generated during reionization which scatter and damp CMB anisotropies, producing a suppression for $\ell > 10$ of $e^{2\tau}$. It is given by:

$$\tau = n_H(0)c\sigma_T \int_0^{z_{max}} dz \frac{n_e^{reion}(z)}{n_H(z)} \frac{(1+z)^2}{H(z)} \tag{41}$$

with:

- σ_T the Thomson cross section

- $n_H(z)$ the total number of hydrogen nuclei
- n_e^{reion} the number density of free electrons of free electrons from reionization
- z_{max} a redshift chosen to be sure that all scattering is taken into account ~ 50

4 Modeling tools

4.1 Intrinsic Alignment

A key assumption in cosmic shear measurements is that the the orientation of intrinsic ellipticities of galaxies is random, so that a statistical alignment observed in neighbouring galaxies can be attributed to cosmic shear. It appeared clearly in the 2000's that while this picture is not wrong, there was a serious caveat to be introduced which was coined "Intrinsic Alignment". Intrinsic Alignment, as its name indicates, is the alignment of neighbouring galaxies due to Tidal Forces coming from the structure in which they formed. The structures producing an Intrinsic Alignment can be filaments, halos or the border of voids as represented in the pictures Fig.13, Fig.14 and Fig.15. While the Intrinsic Alignment signal can contain a lot of physical information on the formation and configuration of structure, it is treated as a systematic error, which has to be taken into account in the modeling of the signal.

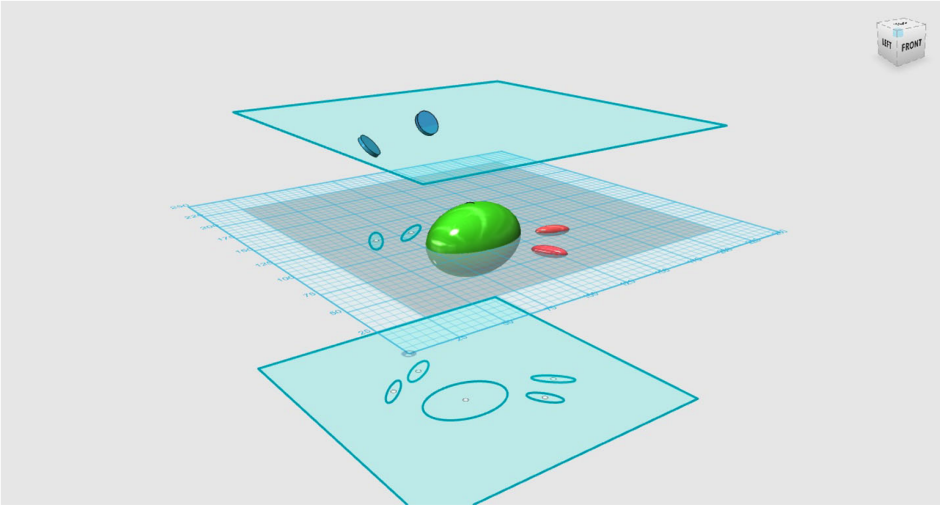

Figure 13: The galaxies in red are subject to forces that make them point towards the structure (in green), this is the Intrinsic-Intrinsic component of the signal, which results in a positive correlation of the alignments. The Galaxy-Galaxy signal is due to the distortion of the light of the blue galaxies by the structure, which produces a positive correlation in the alignment. Finally the Intrinsic-Galaxy component is the anti-correlation between the red galaxy "pointing" towards the structure, while the light of the blue galaxy is compressed tangentially by the structure. source: [Joachimi et al., 2015]

For a review of different modeling approaches of Intrinsic Alignment see [Krause et al., 2016] or [Jagvaral et al., 2022] for an astrophysical subtle distinction. Here we used the strategy of [Hildebrandt et al., 2017], with the decomposition as in Equ.(1) from [Heymans et al., 2021]:

$$C_{\epsilon,\epsilon}^{(ij)}(\ell) = C_{G,G}^{(ij)}(\ell) + C_{G,I}^{(ij)}(\ell) + C_{I,G}^{(ij)}(\ell) + C_{I,I}^{(ij)}(\ell) \tag{42}$$

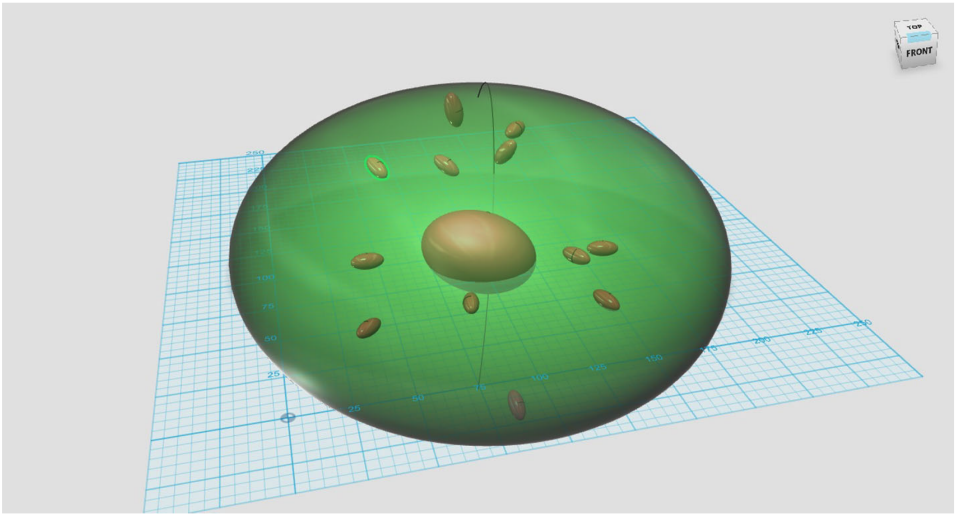

Figure 14: Intrinsic Alignment in a cluster, satellite galaxies tend to point towards the center of the cluster, source: [Joachimi et al., 2015]

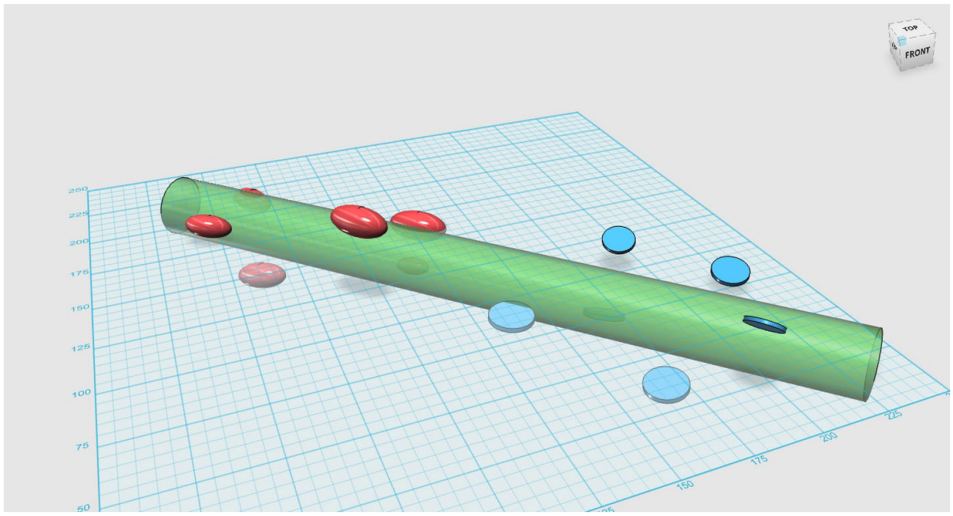

Figure 15: The filament (in green) produces an alignment as galaxies around it will be subject to its tidal forces, source: [Joachimi et al., 2015]

The ij subscript denote the correlation between two redshift bins. The G and I stand respectively for "Galaxy" and "Intrinsic". The GG term is the one carrying the cosmological information, as it represents the correlation due to lensing distortions from the matter field. The II term is the correlation coming from the alignment of two galaxies with the structure, in the case of Fig.13 it is the alignment of the two red galaxies that point towards the bulk of the halo. This contribution is positive as it will have a tendency to correlate the alignment of galaxies.
The IG term on the other hand gives a negative contribution to the $C(\ell)$, it models the anti-correlation coming from the alignment of a galaxy with the halo which is perpendicular to the lensing of the light produced by the halo. In Fig.13 it can be understood by the fact that the light of the blue galaxy gets most strongly distorted along its minor axis which is perpendicular to the

alignment of the red galaxy with the halo center.
The weight of the GI, IG and II terms are modelled using:

$$F(z) = -A_{IA} C_1 \rho_{crit} \frac{\Omega_m}{D_+(z)} \left(\frac{1+z}{1+z_0}\right)^{\eta} \left(\frac{\bar{L}}{L_0}\right)^{\beta} \tag{43}$$

The parameters are:

- A_{IA} the Amplitude of the Instrinsic alignement
- C_1 a constant factor to fit simulations
- $D_+(z)$ the linear growth factor
- L the luminosity and L_0 a pivot luminosity

This formula takes into account the Tidal Forces acting on galaxies in haloes as presented in [Hirata and Seljak, 2010]). We would like to give a brief outline of the origin of this formula.
When placed in a field with a newtonian potential Ψ_p, the tidal force in the $\{x, y\}$ plane produces the mean ellipticity presented in [Catelan et al., 2001]:

$$\epsilon_+ = C(\partial_x^2 - \partial_y^2)\Psi_p \ , \epsilon_\times = 2C\partial_x\partial_y\Psi_p \tag{44}$$

One takes the second derivatives as it changes the shape of the galaxy, while the first derivative $\vec{g} = \nabla\Psi_p$ only shifts the galaxy uniformly. The modification of the shape is presented in Fig.16. It is interesting to note that this deformation acts both on halos and galaxies. Higher order derivative terms are neglected.

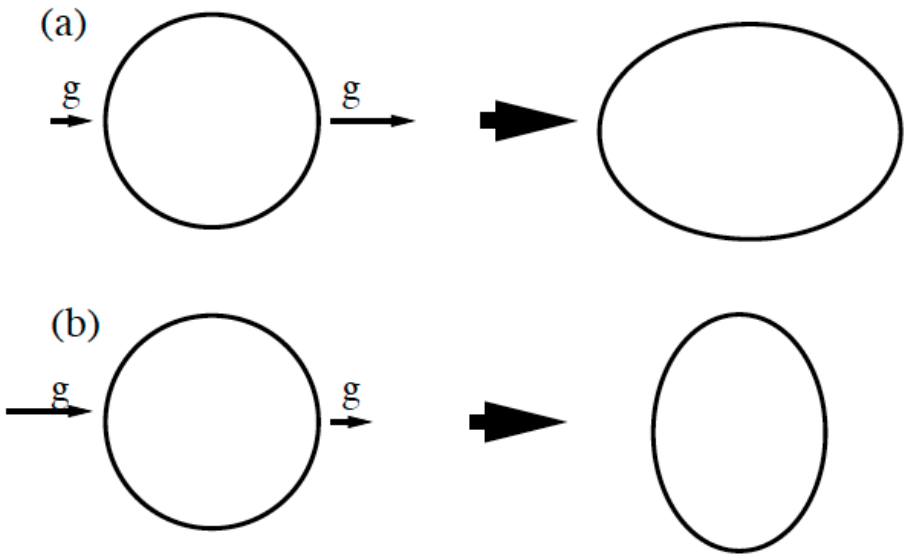

Figure 16: (a) represents the elongation of a halo, (b) shows a compression of the halo from tidal forces

In [Hirata and Seljak, 2010] the intrinsic shear of the galaxy is therefore:

$$\gamma^I = -\frac{C_1}{4\pi G}(\nabla_x^2 - \nabla_y^2, 2\nabla_x\nabla_y)\mathcal{S}[\Psi_p] \tag{45}$$

Where $\mathcal{S}$ is a smoothing filter which cuts-off fluctuations on galactic scales.
The primordial gravitational potential in Fourier space can be written:

$$\Psi_p(k) = -4\pi G \frac{\bar{\rho}(z)}{\bar{D}(z)} a^2 k^{-2} \delta_{lin}(k) \tag{46}$$

It is this linear evolution of the gravitational potential which allows for the simple form of this modeling. Taking the correlation function of the intrinsic shear is what produces the $F^2(z)$ contribution in $C_{I,I}(\ell)$ and the presence of the growth factor, the matter density and the multiplication by the linear or non-linear matter power spectrum. As the corellation function are in Fourier space the derivatives become simple factors of k.
In our analysis we use A_{IA} as the free parameter and fix $\eta = 0$ and $\beta = 0$ in accordance with [Hildebrandt et al., 2017]. We fit A_{IA} using:

$$C_{I,G}(\ell), C_{G,I}(\ell) \propto F(z) \; ; \; C_{G,G}(\ell) \propto F(z)^2 \tag{47}$$

Which should appear clearly from the discussion above.
We plotted the contribution of the different components in Fig.17 using a standard cosmology. From the figure it appears clearly that the Intrinsic-Intrinsic contributions are quite small, while the Galaxy-Intrinsic contribution has an impact, in particular in the low-redshift bins where the tidal field has an effect on the bending of the light as well as the distortion of the foreground lens galaxy.

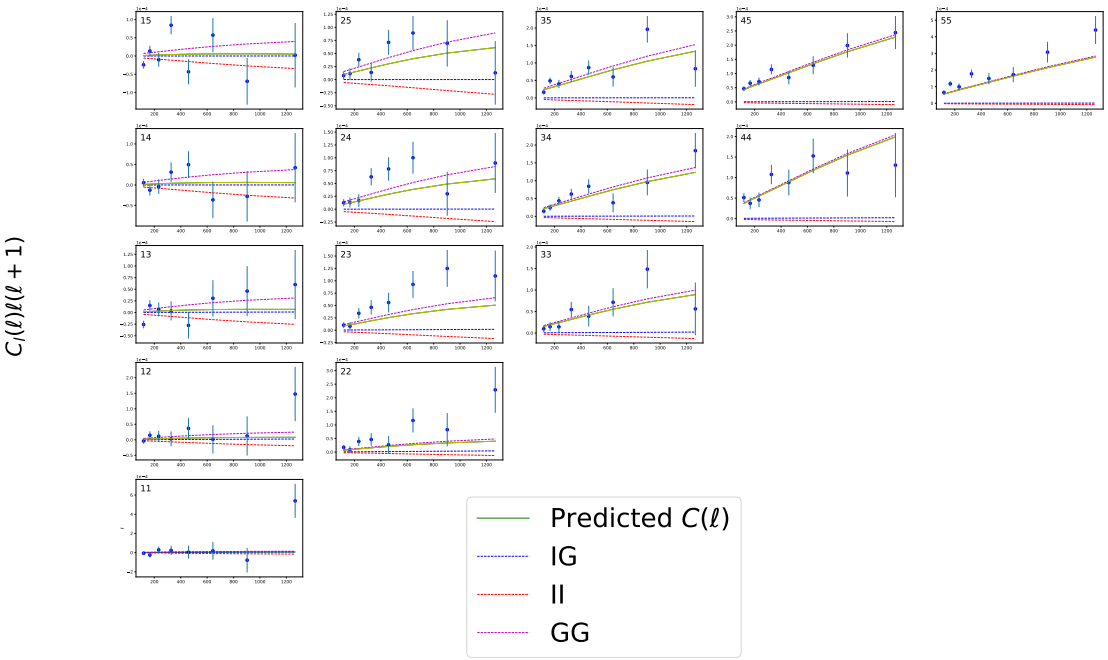

Figure 17: The decompostion of the angular power spectrum in GG, GI, II and the KiDS-1000 data points

In this work we only model the E-modes contributions to the angular power-spectrum. The difference between E and B-modes are analogous to the Electromagnetical divergence and curl. The difference

between E-mode and B-mode distributions of galaxies in the sky is presented in Fig.18. The B-mode contributions to the $C(\ell)$ is theoretically 0, and therefore represents an interesting test to determine the presence of unaccounted systematic errors in the cosmic shear correlation functions.

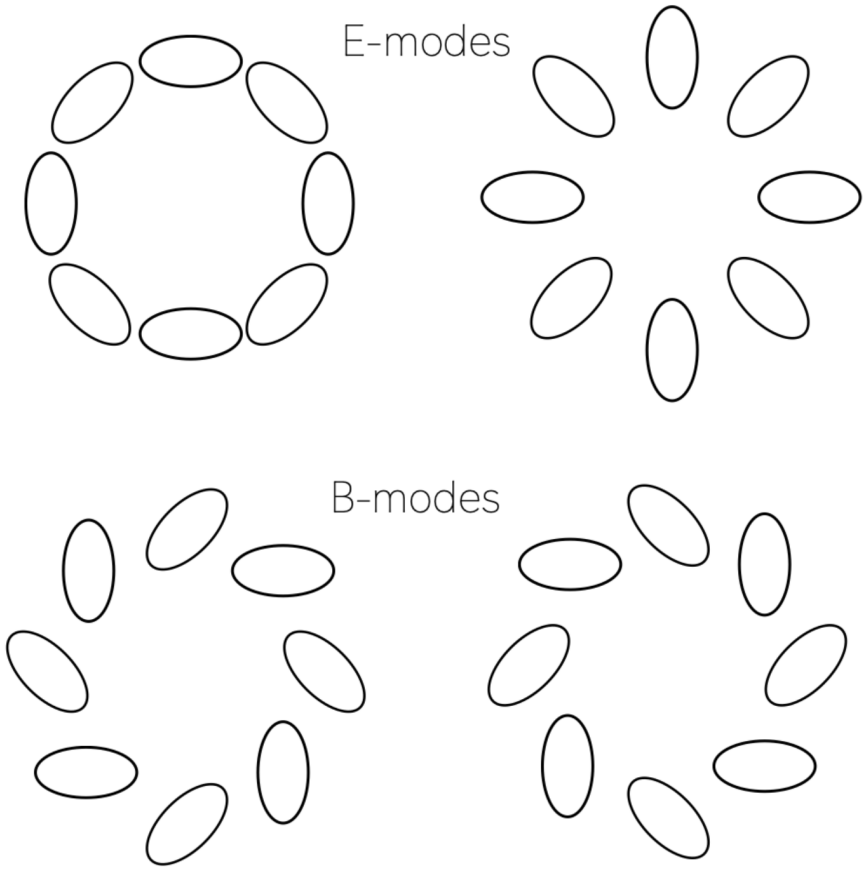

Figure 18: The E and B modes in distributions of galaxies

4.2 N-body simulations

When studying the formation of the Universe and the Large Scale Structure, the main tool to account for gravitational interactions producing a departure from linear perturbation theory has been the use of N-body code simulations. These codes simulate the clustering of very large particles that are only subject to Newtonian gravitational forces in an expanding space-time. They are used to account for the modification of the power spectrum coming from the gravitational interaction of matter and the resulting formation of structure in the matter-dominated era. The gravitational effect in the cold dark matter paradigm produces an excess in the power spectrum starting at $k \sim 0.1h/\mathrm{Mpc}$ and going down to smaller scales. The use of simulations is therefore an expensive but precise method to get a prediction of the observed correlation functions on smaller scales. While these simulations are numerically and computationally very involved we can lay-out their functioning structure.
I) As an input the user has to provide a Transfer function, referred to as $T(k)$ coming from the linear theory which gives the amount of clustering at the starting redshift, which is in the matter-dominated era and can broadly go from $z_{ini} = 100$ to $z_{ini} = 5$. The velocities of the particles must

be non-relativistic at z_{ini}.
II) The particles are initialized according to the transfer function to match the clustering described by the linear Transfer function. The particles are provided with peculiar initial velocities calculated using Lagrangian Perturbation theory at first or second order. These velocities reflect local gravitational flow and are distinct from the thermal velocities $v_{therm} \sim \langle p \rangle / m \sim T/m$ which are particularly relevant for light dark matter particles.
III) The particles are then evolved forward step by step with the gravitational force either calculated between two close particles or between a particle and the center of a cell in which the masses of the particles have been summed over for particles that are further away. Note that different N-body code algorithms are mainly distinguished by the way the cells are partitioned and averaged over.
IV) The positions of the particles are then updated based on their new velocity resultant of the gravitational acceleration they received. The underlying space is not a constant frozen lattice but it evolves based on the specified cosmology, which is referred to as the "background evolution".
V) When the desired redshift of the observation has been reached, the power spectrum can be quite easily computed by producing a distribution of the distance between particles. Note that the particles in a N-body simulation have a mass of the order 10^9 solar masses and therefore represent a cluster of stars or a large dark matter quantity.
The N-body codes therefore allow to understand the increase of the non-linear power spectrum in smaller ranges due to the gravitational clumping of matter. By considering that all matter only interacts gravitationaly, the physical picture is simplified as the electromagnetic interaction of baryons and the different astrophysical process they produce are unaccounted for.

4.3 Baryonification and the Baryonic Emulator

To correct for the effect of baryons on the simulation, a lot of effort has been devoted in recent time, using hydrodynamical simulations to get a better quantification of the induced suppresions. One approach developed in Teyssier and Schneider [Schneider and Teyssier, 2015] has been the baryonification process.
In this framework the particles in N-body simulations are slightly shifted in their final position to match a corrected halo profile. The correction is physically motivated to contain the ejection of gas by Active Galactic Nuclei (AGN) and stellar feedback.
The standard halo profile is the *dark matter only* case:

$$\rho_{dmo}(r) = \rho_{nfw}(r) + \bar{\rho}_{bg} \tag{48}$$

where NFW stands Navarro-Frenk-White profile, which is a very commonly used halo profile describing the density of matter at a given radius of the halo, and $\bar{\rho}_{bg}$ is the background density which has not collapsed to form halos yet.
The corrected final profile given by the *baryonic correction model* is:

$$\rho_{bcdm}(r) = f_{rdm} y_{rdm}(r) + f_{bgas}(M) y_{bgas}(r) + f_{egas}(M) y_{egas}(r) + f_{cgal}(M) y_{cgal}(r) + \bar{\rho}_{bg} \tag{49}$$

where the contributions to the halo-profile have been decomposed in:

- *rdm* the relaxed dark matter
- *bgas* the gas bound in the halo, in hydrostatic equilibrium
- *egas* the expelled gas due to ejection from any feedback process

- *cgal* the stellar component of the central galaxy

The y_i represent the individual normalized profile, f_i the corresponding fractions and M is the enclosed mass.
This method is very interesting as it is computationally cheap to slightly modify N-body codes outputs to contain baryonic effects, compared to the running of a full hydrodynamical simulation.
When modeling our data, we want to vary the different contributions from the baryonic parameters, to constrain them and accurately model our power-spectrum on the smaller scales.
Unfortunately we can not run an N-body simulation for each set of parameters, as that would be computationally too expensive and we therefore need an efficient tool to extract the corrections corresponding to our choice of parameters.
To that end we use an emulator [Giri and Schneider, 2021], which was built to model the suppression of the baryonic corrected dark matter profiles using 7 parameters. These parameters modify the shape of the profiles contributing to the *baryonic correction model* . In particular the profile for the central galaxy:

$$\rho_{cga}(r) = \frac{f_{cga}(M)}{4\pi^{3/3} R_h r^2} \exp\left[-\left(\frac{r}{2R_h}\right)^2\right] \tag{50}$$

and the gas profile:

$$\rho_{gas}(r) \propto \frac{[\Omega_b/\Omega_m - f_{star}(M)]}{\left[1+10(\frac{r}{r_{vir}})\right]^{\beta}(M)\left[1+(\frac{r}{\theta_{ej} r_{vir}})^{\gamma}\right]^{\frac{\delta-\beta(M)}{\gamma}}} \tag{51}$$

with β having the Halo mass dependence:

$$\beta(M_c, \mu) = \frac{3(M/M_c)^{\mu}}{1+(M/M_c)^{\mu}} \tag{52}$$

Therefore these profiles have 7 physical parameters that can be finetuned with:

- $(log_{10}M_c, \mu, \theta_{ej}, \gamma, \delta)$ give the shape of the gas profiles from Equ.51 and Equ.52
- (η, η_δ) give the stellar abundance in the satellite galaxies and central galaxies respectively.
- $f_b = \Omega_b/\Omega_m$ gives the ratio between baryonic matter and total matter

The model has been tested to accurately reproduce the suppression from baryons in hydrodynamical simulations. In Fig.19 are plotted angular power spectra for arbitrary choices of baryonic parameters. While the modifications induced by the baryonic correction models seem similar to those coming from a mixed dark matter scenario, their redshift dependence is the opposite with the baryonic corrections getting stronger as redshift lowers while the Mixed dark matter effects get smoothed out. Deeper surveys going to higher redshifts should therefore be very efficient to uncorrelate these effects.

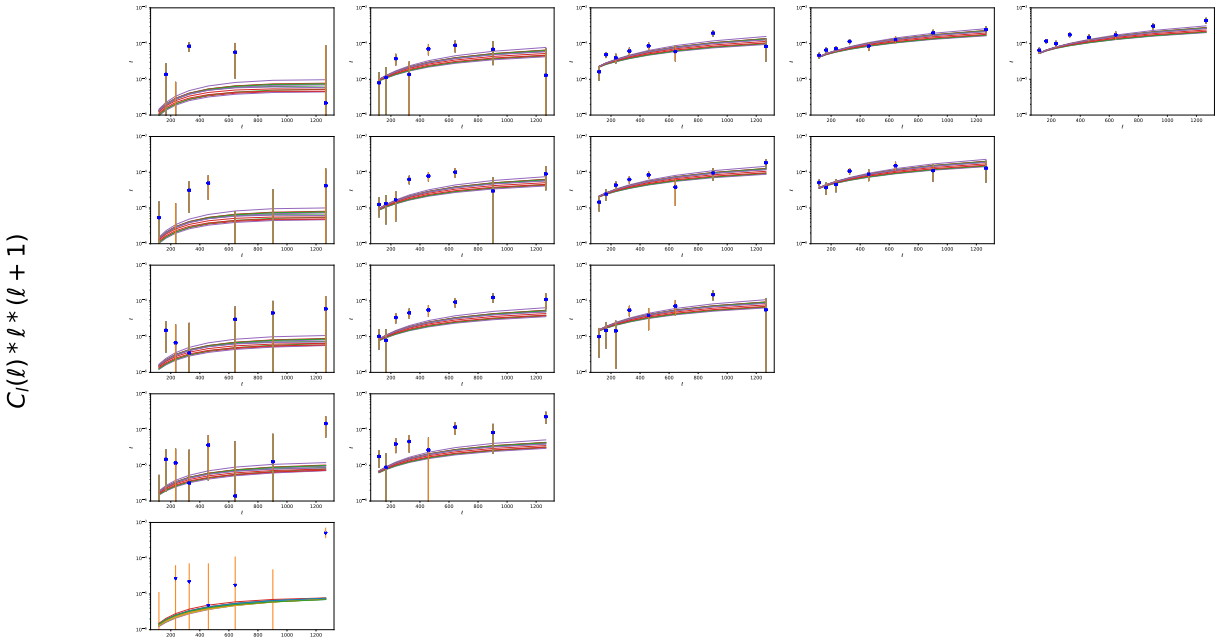

Figure 19: suppression in the angular cosmic shear $C(\ell)$ from randomly selected baryonic parameters

4.4 Mixed dark matter emulator

In the linear theory, the perturbations have been worked out during the second half of the XXth century. For a full review which includes hot dark matter we refer the reader to [Ma and Bertschinger, 1995]. The non-linear modification in the mixed dark matter scenario can not be computed analytically and therefore need to be estimated using previously described N-body simulations. To predict suppression in the non-linear-power spectrum from mixed dark matter we use the emulator presented in [Parimbelli et al., 2021] which is a central part of this work and we will therefore describe it in detail.

This emulator is built upon a suit of simulations which samples the $\{f_{wdm}, m_{wdm}\}$ parameter space. The simulations use a Transfer function input at $z = 99$, which as explained in section 4.2 produces a starting position of the N-body simulation which matches the linear theory. The transfer functions generated with CLASS are the only difference between the simulations. The initial conditions are produced using second-order Lagrangian perturbation theory. Once the simulations have been run, a Principal Component Analysis is used to reduce the problem to twenty dimensions. A Gaussian Process Regression is then applied to predict the suppression in the power spectrum.

The emulator is trained using 60 simulations (yellow in Fig.20), a few simulations are reserved to test the extrapolation capacity of the emulator. The idea is that any parameter-combination in a reasonable proximity to a training point can be predicted using the emulator. The suppression in the non-linear power spectrum for different masses and fractions are presented in Fig.21 and Fig.22 for redshifts 3 and 0 respectively. Note that we imposed the correction to always be below 1 as we took the bump at smaller k to be caused by unphysical resolution effects.

The effect on the $C(\ell)$'s of different masses and fractions is shown in Fig.23 and Fig.24

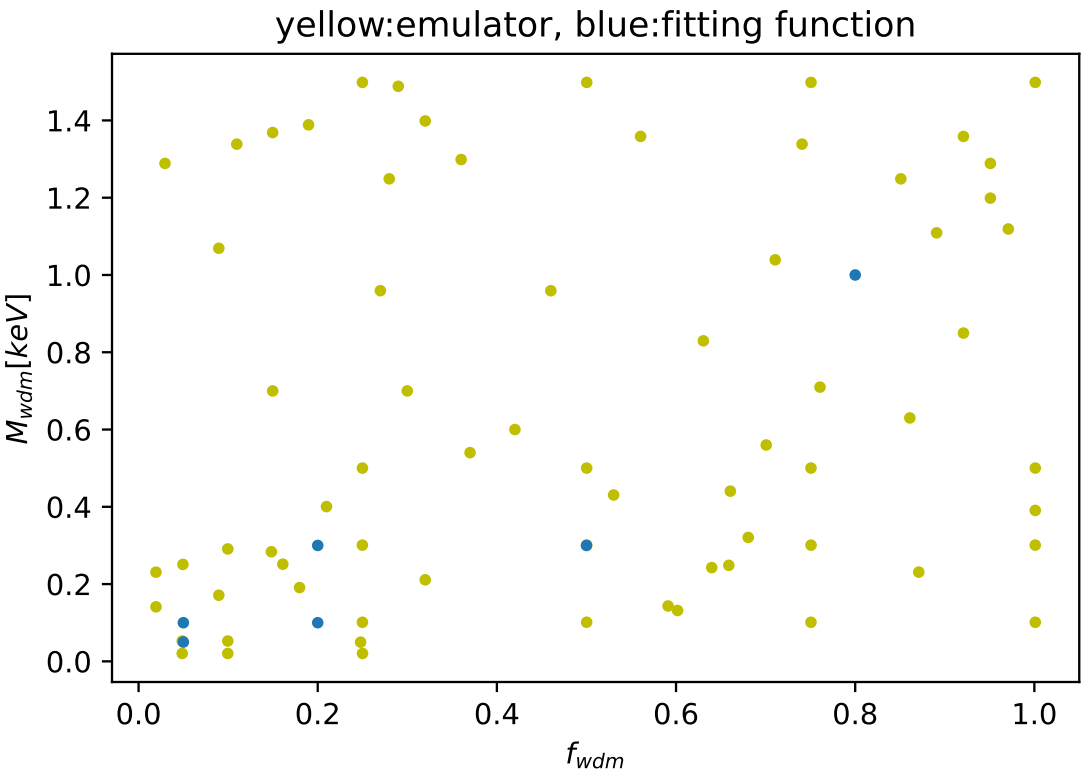

Figure 20: The training points for the emulator of [Parimbelli et al., 2021] in yellow and the fitting function of [Kamada et al., 2016] in blue

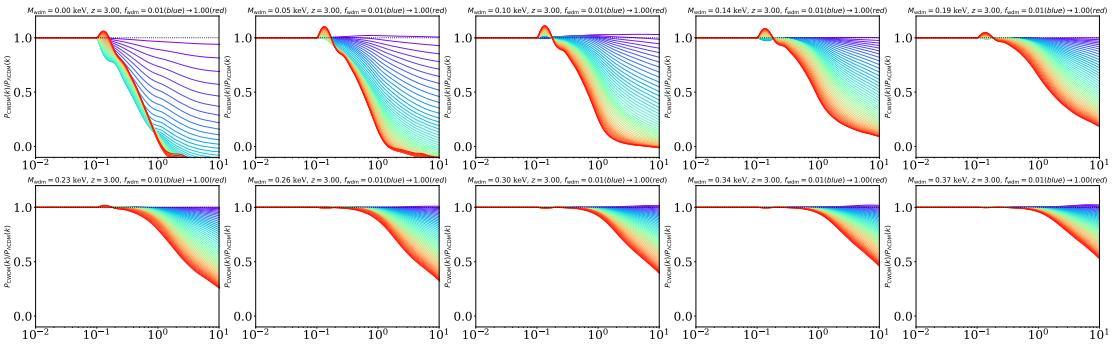

Figure 21: The suppression in the non-linear power spectrum from Mixed Dark matter with respect to the ΛCDM non linear power sepctrum at z=3,k in h/Mpc

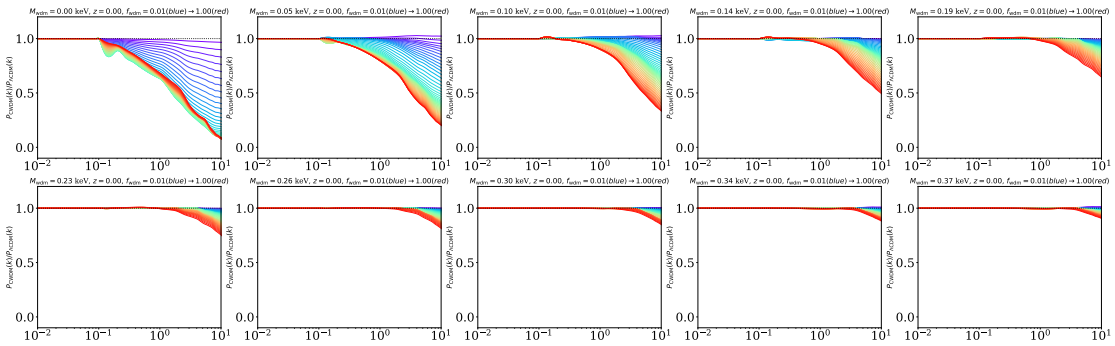

Figure 22: The suppression in the non-linear power spectrum from mixed dark matter with respect to the ΛCDM non linear power spectrum at z=0, k in h/Mpc

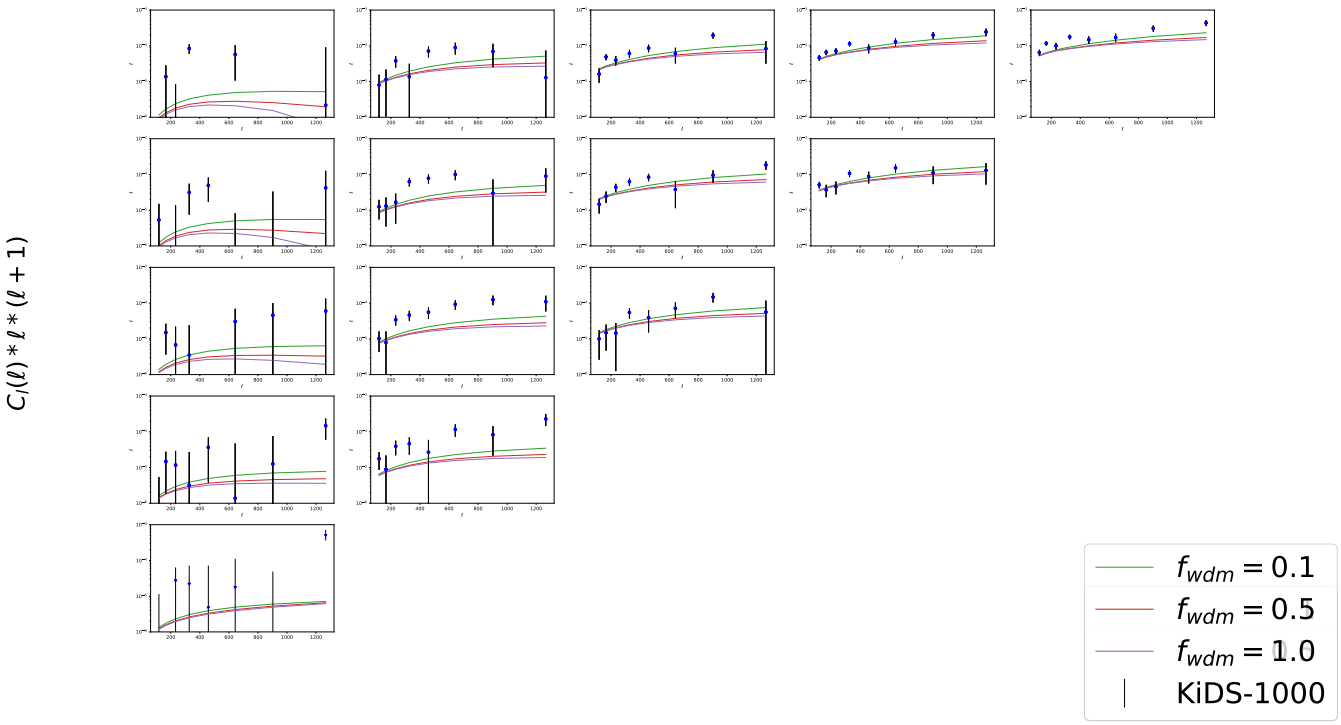

Figure 23: The suppression in the angular spectrum from mixed dark matter with $m_{wdm} = 0.05$keV

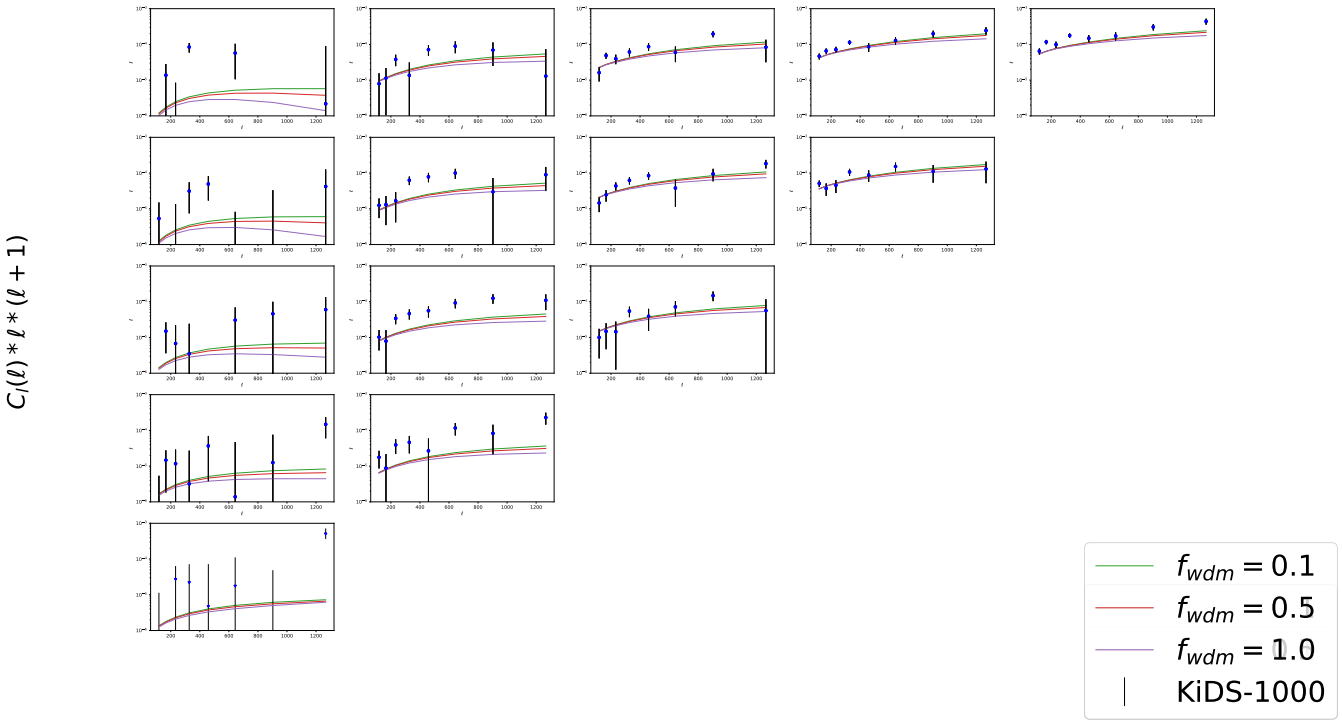

Figure 24: The suppression in the angular spectrum from mixed Dark matter with $m_{wdm} = 0.1$keV

4.5 Comparison to a fitting function

We did not run any simulations as a test to determine the accuracy of the emulator independently but we could compare the emulator to a previously computed fitting function. The principle of the fitting function is to sample a similar parameter space, but instead of doing a gaussian process regression, the power spectrum suppression is predicted using a physically motivated fitting function with parameters tuned to match a few simulations in the desired parameter space. The fitting function is presented in [Kamada et al., 2016].

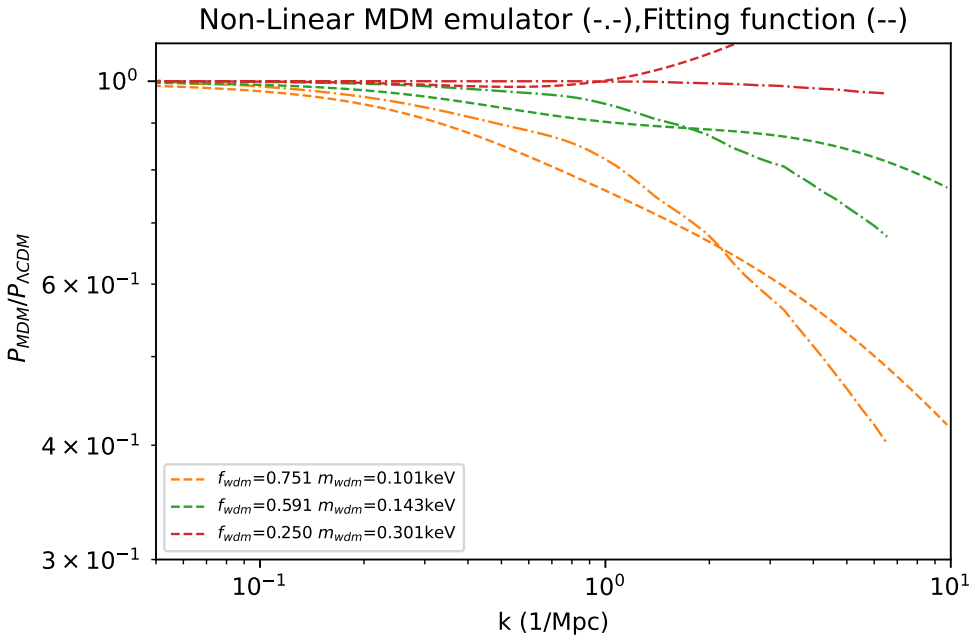

Figure 25: comparing the fitting function and emulator at values on which the emulator has been trained

For the fitting function, we define the quantity:

$$r_{warm}(f_{wdm}) = 1 - \exp\left(-a\frac{f_{wdm}^b}{1-f_{wdm}^c}\right) \tag{53}$$

This new quantity contains the parameters a, b, c which are the free parameters fitted to match the simulations.
We also need a damping scale associated to the free streaming scale:

$$k_d(m_{wdm}, z) = 388.8h/\text{Mpc}(\frac{m_{wdm}}{\text{keV}})^{2.207}D(z)^{1.583} \tag{54}$$

Which is rescaled with $f_{wdm}^{-5/6}$ in accordance with the Jeans length, which means $k'_d = k_d/f_{wdm}^{-5/6}$.
We can finally bring all these elements together to get the non-linear suppression in the power spectrum :

$$\frac{P_{nl,MDM}}{P_{nl,\Lambda CDM}} = (1 - r_{wdm}) + \frac{r_{wdm}}{(1 + k/k'_d)^{0.7411}} \tag{55}$$

We present in Fig.25 the match or mismatch between the emulator approach and the fitting-function approach.

4.6 Monte-Carlo-Markov-Chains

To model the signal we construct a pipeline to reconstruct the data points as they are given by the KiDS-1000 and the Planck-18 measurements. In our model we use parameters that can be varied to change each effect. We allow these parameters to vary inside bounds called priors. The prior can be "top-hat" which means we are agnostic about where in the allowed range the best fit value lies, or "gaussian" where a preferred value is indicated with a gaussian spreading.
The Monte-Carlo-Markov chain generates a random walk over the parameter space. The goal is to draw samples $\{\Theta_i\}$ to understand the posterior probability density, using the prior and the likelihood function:

$$p(\Theta, \alpha|D) = \frac{1}{Z} p(\Theta, \alpha) p(D|\Theta, \alpha) \tag{56}$$

Z is a normalization we do not need to compute as we can probe the relative change in the likelihood. The prior $p(\Theta, \alpha)$ is explained above and the likelihood $p(D|\Theta, \alpha)$ is what is calculated on every-step (in fact we evaluate the log-likelihood) to probe the correspondence between the sample and the data. The variables Θ and α are to be understood as model parameters and nuisance parameters respectively.
To obtain the posterior, a chain is run according to the Metropolis-Hastings algorithm, which accepts or rejects each step according to the likelihood and the use of a randomly varying threshold. The initiation of the parameters of the chain is random and we therefore discard an initial fraction of the chain, typically between 20 and 50% as they probe parameter points that are not included in our final steady distribution. To run the chains we use the module emcee [Foreman-Mackey et al., 2013].

5 Analysis

5.1 Pipeline of the KiDS-1000 Data

As described in section 3.1 our goal is to model the Angular-power spectra retrieved from [Asgari et al., 2021], using the mixed dark matter theory.
An overview of the pipeline is given in Fig.26.
For the modeling of the cosmic shear signal we start by calculating the linear power spectrum $P_{lin}(k)$ using CLASS, with the parameters $\{\omega_m, A_S\}$ being varied by the Monte-Carlo Markov-Chain with priors described in 2. The other main cosmological parameters are fixed to the Planck18 values [Planck col. et al., 2020], in particular: $\Omega_b = 0.049, n_s = 0.966, N_{eff} = 3.046$. We model a massive neutrino with a fixed mass $m_\nu = 0.06eV$. The energy density of the massive Neutrino is given by:

$$\Omega_\nu = \frac{m_\nu}{93.14eV * h^2} \tag{57}$$

Therefore $\Omega_{dm} = \Omega_m - \Omega_b - \Omega_n u$ and $\Omega_\Lambda = 1 - \sum_i \Omega_i$ is matched by CLASS to guarantee a flat Universe.
We then use the revised-halofit fitting function from [Takahashi et al., 2012] which was calibrated to give the non-linear correction to an input Linear Power spectrum for a range of cosmic parameters. In the Halofit model the power spectrum is split in two terms: the one and two halo terms. The two Halo term represents the clustering due to interactions between halos and therefore dominates at larger scale, while the one halo term describes clustering inside a halo and therefore dominates on smaller sales.
Now that we have $P_{nl,\Lambda CDM}$ we can apply the baryonic and mixed dark matter corrections as described in part 3.3 and 3.4 part respectively. For the baryonic parameters we let $\{\eta_d, \theta_j, \log_{10}(M_c)\}$

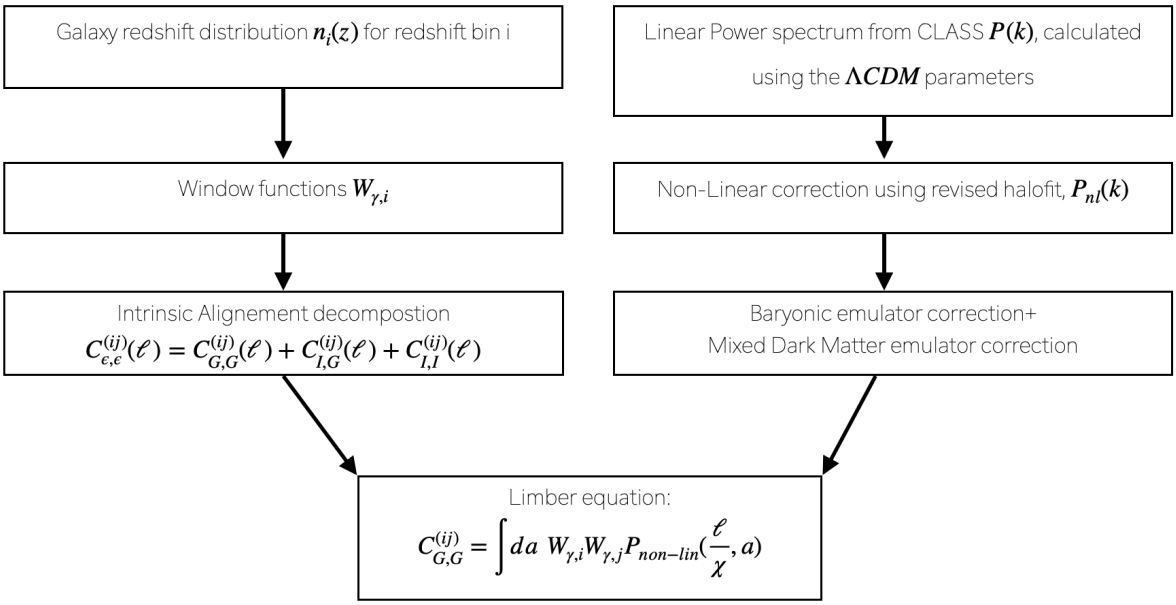

Figure 26: The main blocks of or analysis pipeline

be varied by the chain, while we fix:

$$\mu = 0.7,\ \nu = 0,\ \gamma = 2,\ \delta = 5,\ \eta = 0.25 \tag{58}$$

Finally we update Ω_b/Ω_m in accordance with the choice of parameters of the iteration. Note that the baryonic correction is computed on the whole redshift range:$z \in \{0; 1.5\}$
For the correction due to mixed dark matter we use the emulator which is also computed on the whole redshift range. It is shown in the paper [Parimbelli et al., 2021] that baryonic effets and mixed dark matter suppression can be treated independently (section 3.4.). We show in section 5.3 that this is the case as naryonic parameters are constrained to the same values in ΛCDM and MDM scenarios.
Once the non-linear matter power spectrum P_{nl} has been computed, it needs to be shaped into an angular power spectrum $C(\ell)$ as this is the cosmic shear observable. To do this we use the publicly available PyCosmo code described in [Refregier et al., 2017] and [Tarsitano et al., 2020].
We start by retrieving the publicly available galaxy redshift distributions from [Asgari et al., 2021], represented in Fig.28. As explained in section 3.1, this distributions are not spectrometrically evaluated but are based on the spectrum of the galaxies through the different band-filters. These redshift bins $n_i(z)$ are then used to compute the weight functions:

$$W_\gamma(a) = \frac{3}{2}\Omega_m(\frac{H_0}{c})^2\frac{\chi(a)}{a}\int_{a_{min}}^{a_{max}}\frac{da_s}{a_s^2}n(a_s)\frac{\chi(a_s)-\chi(a))}{\chi(a)} \tag{59}$$

The weight function is slightly more complicated in a curved space.time as $f_\kappa(\chi) = \chi$ is only valid in a flat space-time, which is the only case we consider in this work. The values a_{min} and a_{max} are the scale factors we chose for our integration. In agreement with the KiDS-data we chose a redshift vector $z \in [0.01, 1.5]$ corresponding to a scale factor vector $a \in [0.4, 0.99]$.
Once the weight functions are established, everything can be brought together through the Limber

parameter	prior range
ω_m	[0.44,0.404]
$\log(10^{10}A_s)$	[0.,4.3]
A_{IA}	[-2,2]
$\log_{10}(M_c)$	[11.,15.]
θ_j	[4.,6.]
η_δ	[0.05,0.4]
f_{wdm}	[0.,1.]
$log_{10}(1/M_{wdm})$	[-0.17,2]

Table 2: The top-hat priors used in the KiDS-1000 analysis (the parameters above the horizontal are for the ΛCDM case)

equation described in sect 2.4:

$$C_{G,G}^{(ij)} = \int da\ W_{\gamma,i} W_{\gamma,j} P_{non-lin}(\frac{\ell}{\chi}, a) \tag{60}$$

Note that this is the Galaxy-Galaxy contribution of the signal, the total signal being composed of the Galaxy-Galaxy, Galaxy-Intrinsic and Intrinsic-Intrinsic signals as explained in sect 4.1 and shown in Fig.17. The decomposition is:

$$C_{\epsilon,\epsilon}^{(ij)}(\ell) = C_{G,G}^{(ij)}(\ell) + C_{G,I}^{(ij)}(\ell) + C_{I,G}^{(ij)}(\ell) + C_{I,I}^{(ij)}(\ell) \tag{61}$$

Now that we have a full angular power-spectrum prediction $C_{EE}(\ell)$, we need to account for mode mixing to be fully consistent with [Asgari et al., 2021], which is presented in equation (12) of the aforementioned paper:

$$C_{E,l} = \frac{1}{2\mathcal{N}_l} \int_0^\infty d\ell\ell [W_{EE}^l(\ell) C_{EE}(\ell) + W_{EB}^l(\ell) C_{BB}(\ell)] \tag{62}$$

The B-modes are discarded in our analysis as explained in sect 4.1. The normalization $\mathcal{N}_l$ is calculated for the band powers to trace the centers of the angular power spectra bin, and is defined by:

$$\mathcal{N}_l = \ln(\ell_{up,l}) - \ln(\ell_{lo,l}) \tag{63}$$

where up and low refer to the upper and lower angular Fourier scale (ℓ) of the bin l. The window functions $W_{EE}^l(\ell)$ which accounts for mode mixing in the 8 l bins are extracted from the paper [Joachimi et al., 2021] and represented in Fig.27. Once the integration of Equ.62 is performed, we can finally compute the log-likelihood using the covariance matrix which is publicly available in [Asgari et al., 2021]. For details on how the covariance matrix has been obtained see [Joachimi et al., 2021]
The results of the Monte-Carlo-Markov-Chain are presented in part 5.3

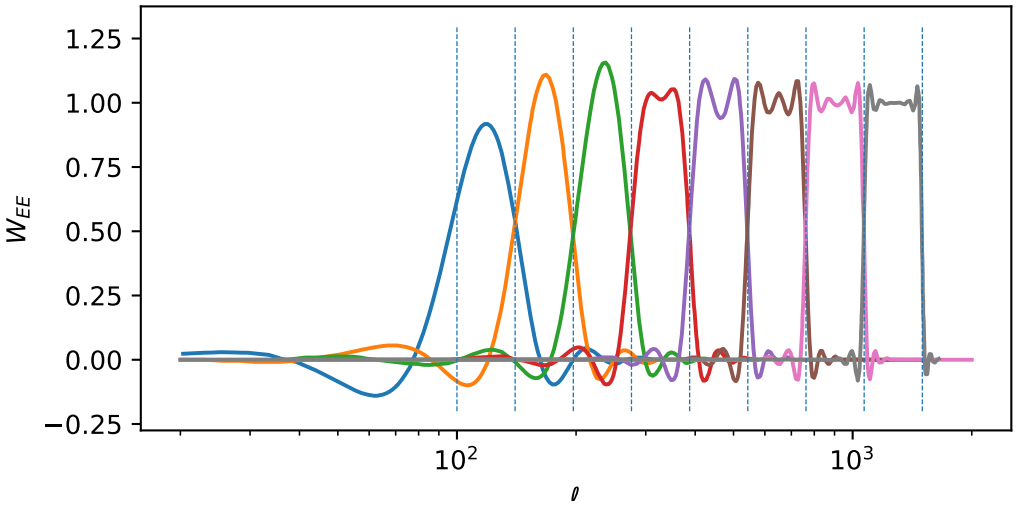

Figure 27: The window functions extracted from [Joachimi et al., 2021] we use to account for mode mixing, the bins are logarithmically spaced with $\ell \in \{100, 1500\}$

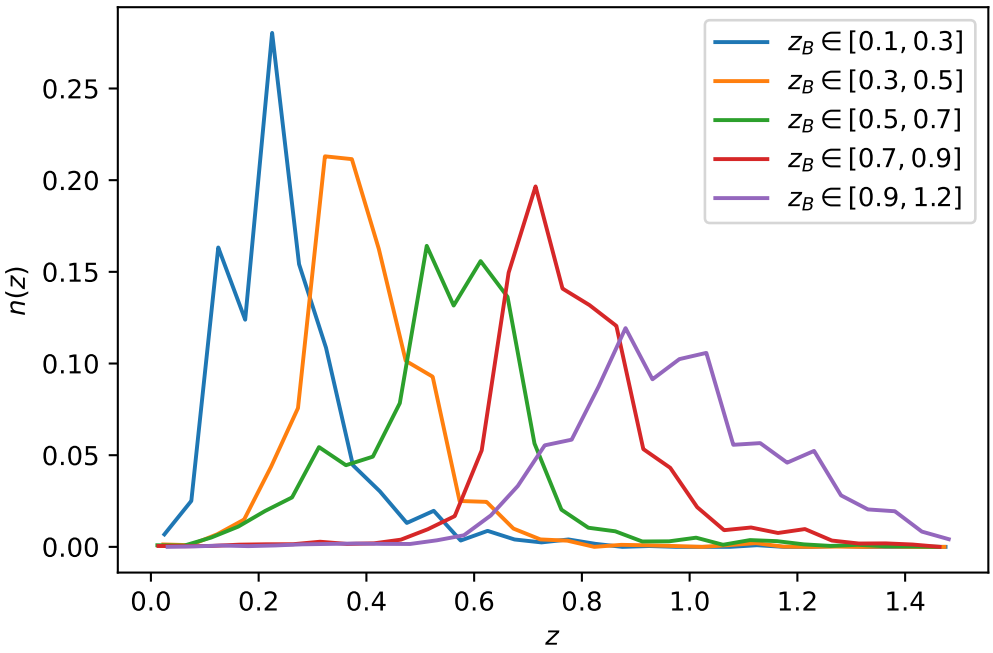

Figure 28: The redshift distribution of the galaxy density in the 5 redshift bins

5.2 Analysis of Planck 18 TTTEEE spectrum

To analyse constraints coming from the Planck 18 dataset we use the Planck-lity-py likelihood presented in [Prince and Dunkley, 2019]. We use the TTTEEE Spectrum with low-ℓ bins. The T stands for Temperature, which is giving by the energy/wavelength of the photon, while E is the

parameter	range
ω_m	[0.44,0.404]
$\log(10^{10}A_s)$	[0.,4.3]
ω_b	[0.01,0.03]
n_s	[0.8,1.3]
τ	[0.03,0.08],$-\frac{1}{2}\frac{(\tau-0.0544)^2}{0.007^2}$
h	[0.5,0.9]
f_{wdm}	[0.,1.]
$log_{10}(1/M_{wdm})$	[-0.17,2]

Table 3: The priors used in the Planck-18 TTTEEE analysis (the parameters above the horizontal are for the ΛCDM case), the prior for τ is a log-gaussian centered on the Planck18 value, all others are “top-hat"

E-mode polarization which is created by Thomson scattering. Including the low ℓ region means including the range $\ell \in [2; 30]$ while the high ℓ's are $\ell \in [30; 2508]$. The power spectra are generated using CLASS and the spectra are lensed, as the effects due to lensing have not been subtracted in the data points. To include our mixed dark matter scenario we provide CLASS with Ω_{ncdm} which is the energy density of non-cold dark matter today and m_{ncdm} which is calculated as $m_{\nu,s}$ according to the conversion in Equ.34. The other parameters varied in the chain are $h, \tau, n_s, A_s, \Omega_m, \omega_b$ which are respectively defined in Equ.6, Equ.41, Equ.39 and Equ.5. The priors are shown in tab.3. From Fig.29 to Fig.34 you can see the effects of mixed dark matter in the different power spectra. The grey bands indicate the uncertainties from in the Planck-18 data.

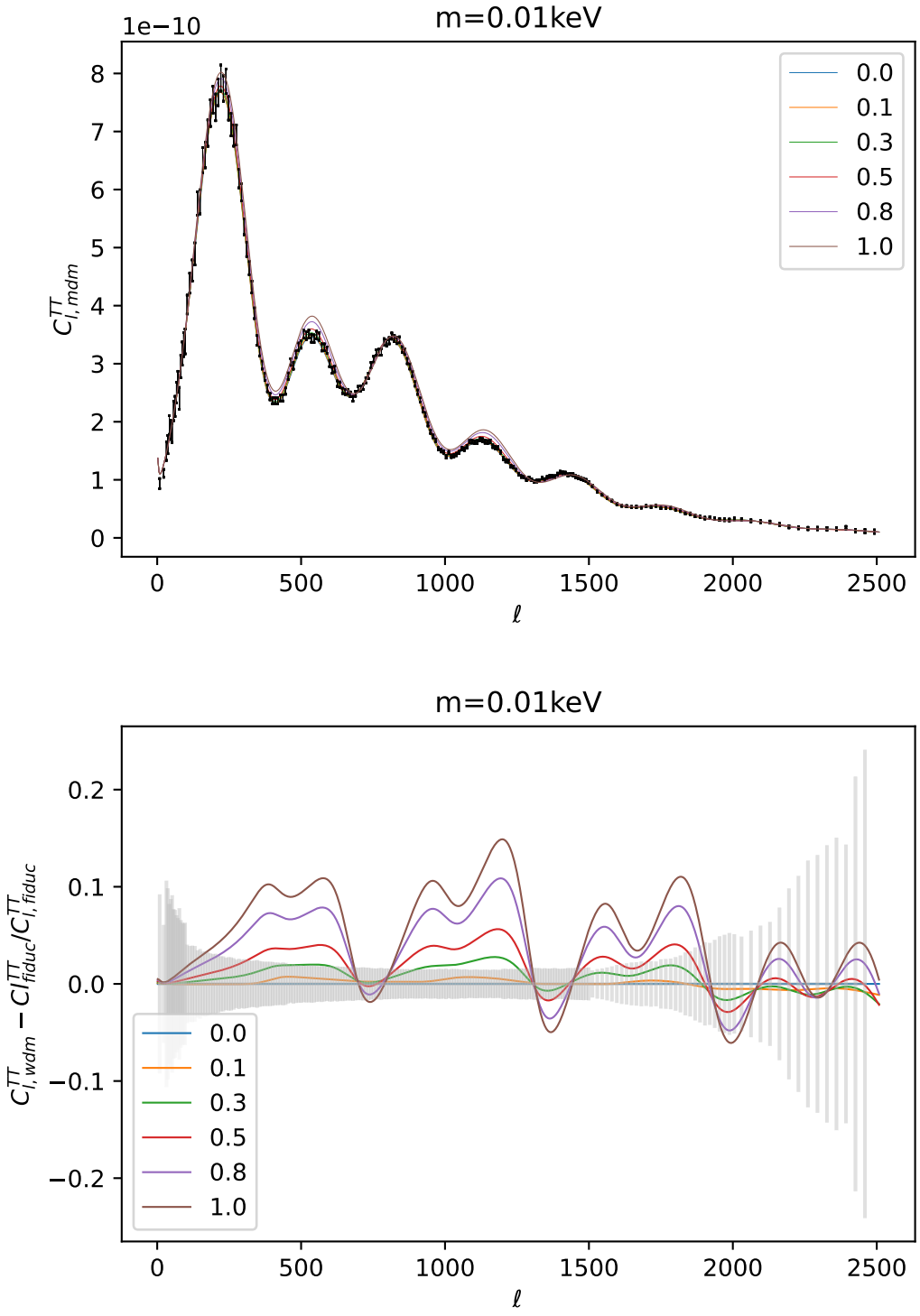

Figure 29: The TT spectrum for $m_{wdm} = 0.01$ keV and various fractions f_{wdm}

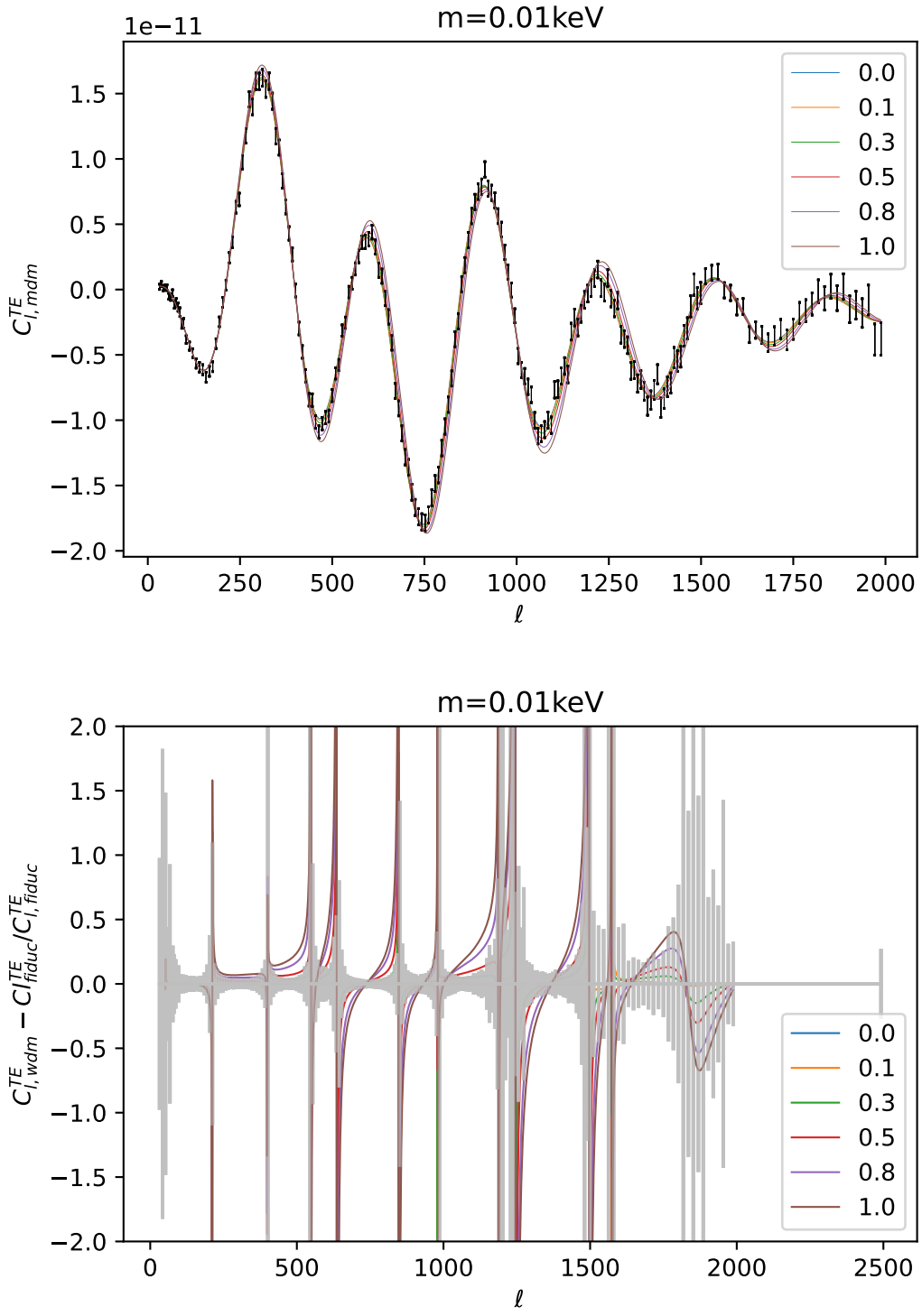

Figure 30: The TE spectrum for $m_{wdm} = 0.01$ keV and various fractions f_{wdm}

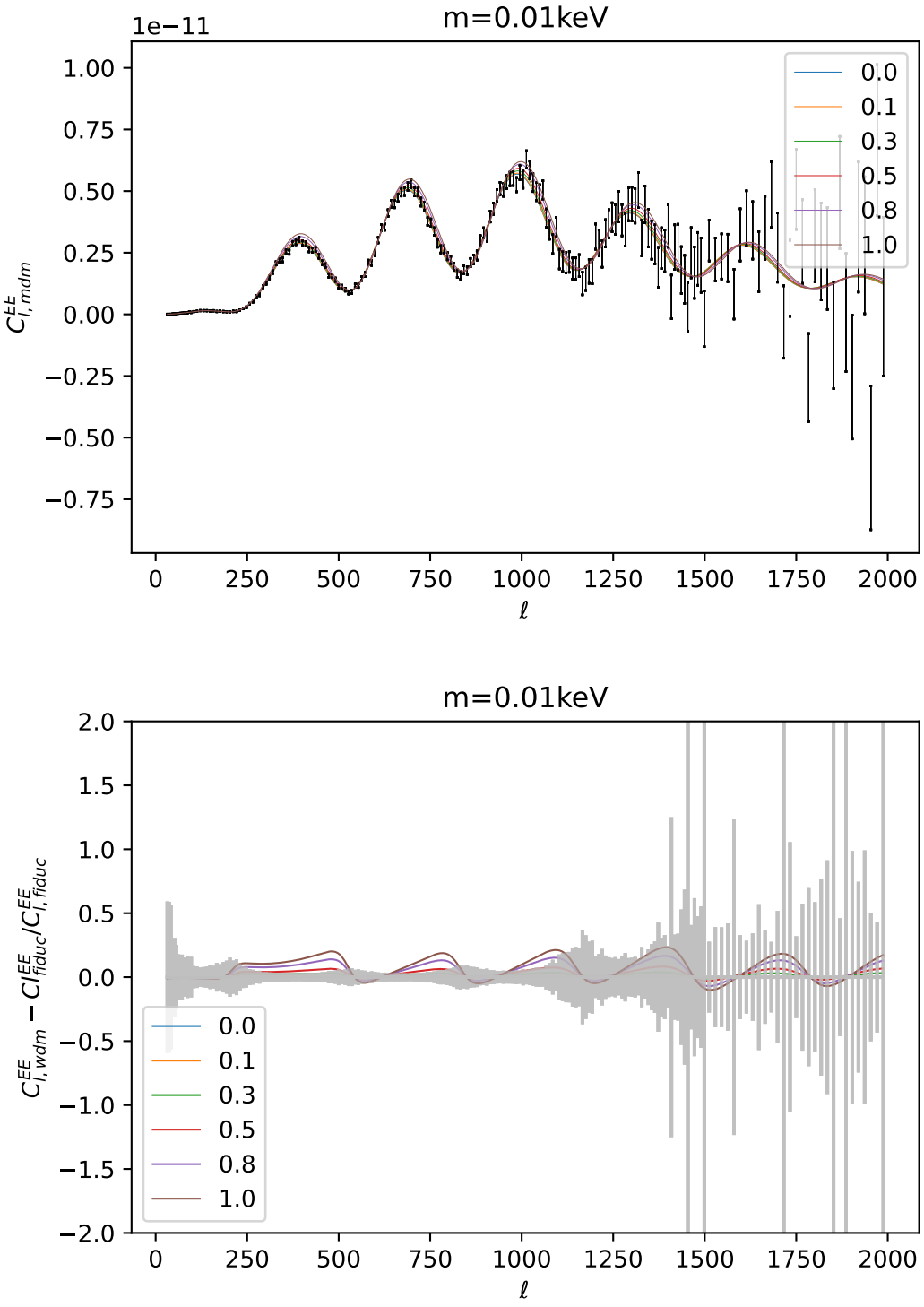

Figure 31: The EE spectrum for $m_{wdm} = 0.01$ keV and various fractions f_{wdm}

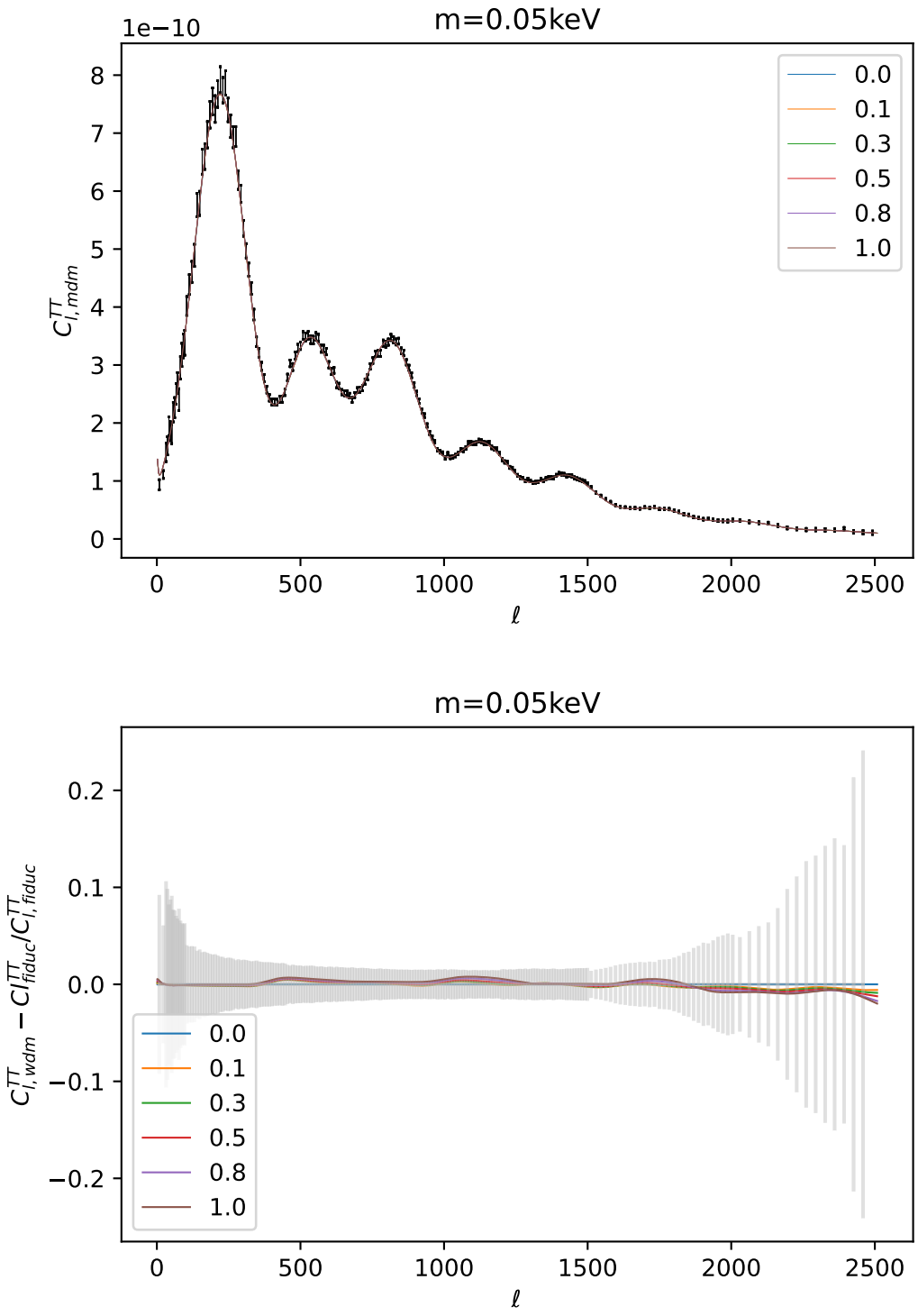

Figure 32: The TT spectrum for $m_{wdm} = 0.05$ keV and various fractions f_{wdm}

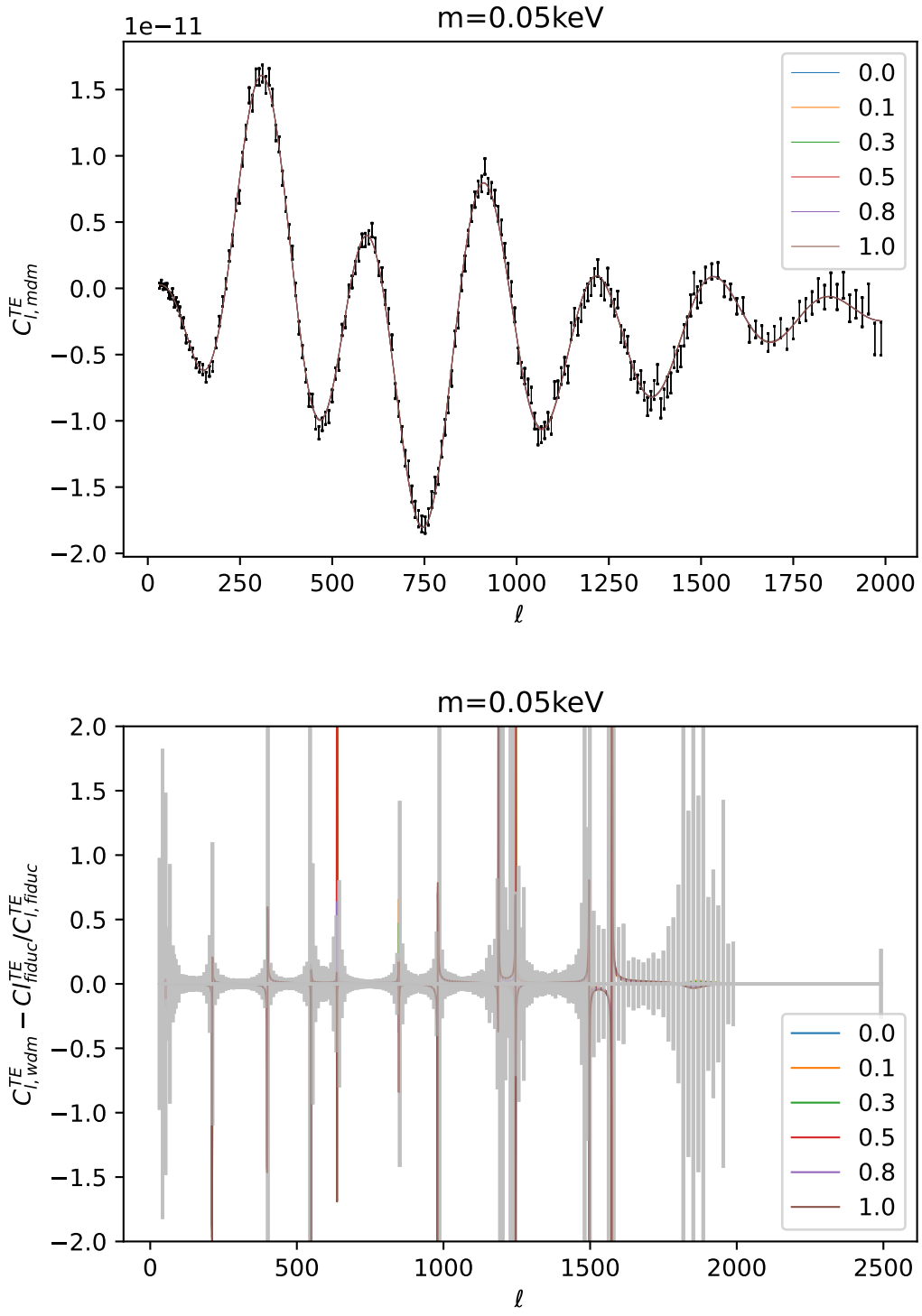

Figure 33: The TE spectrum for $m_{wdm} = 0.05$ keV and various fractions f_{wdm}

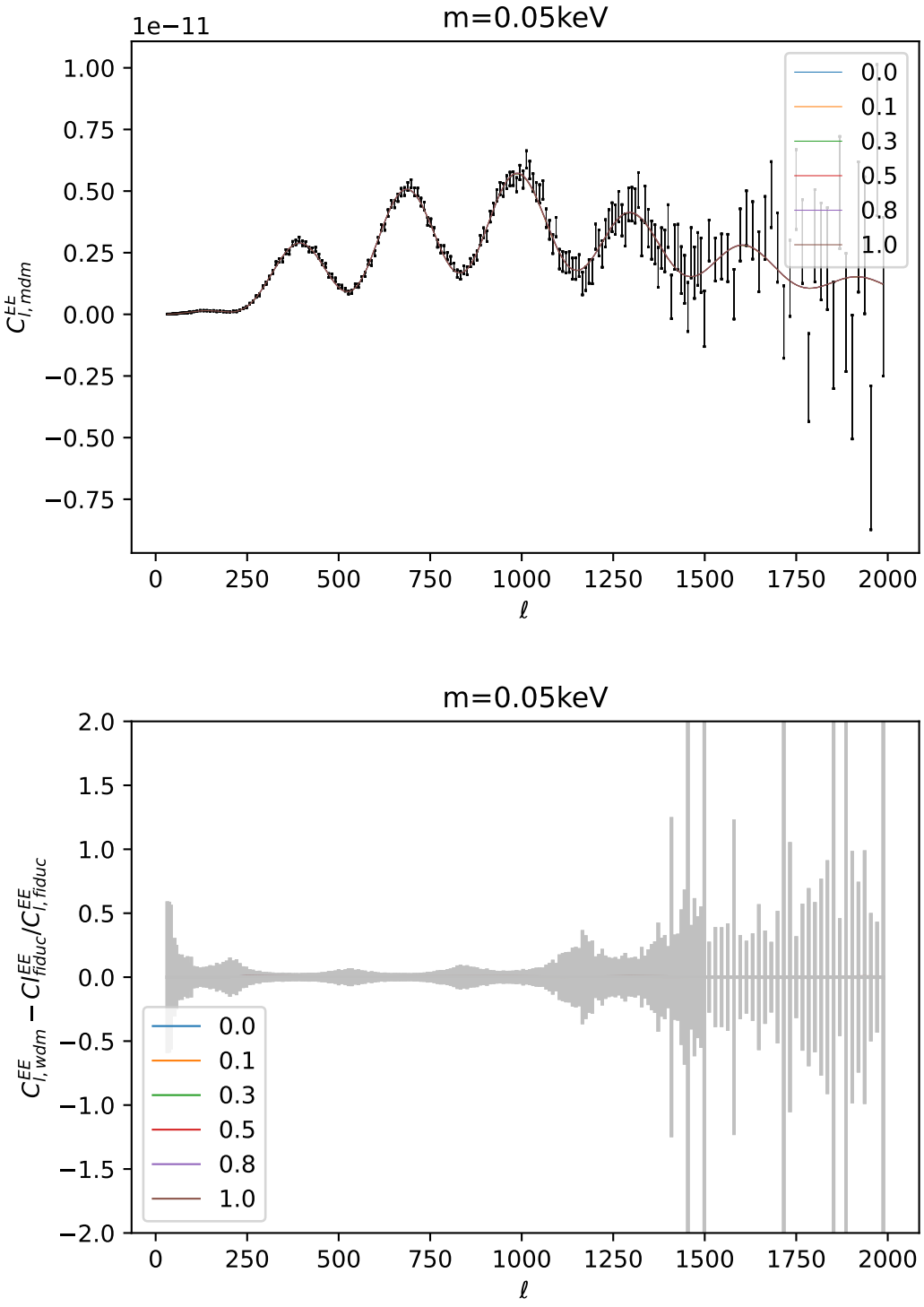

Figure 34: The EE spectrum for $m_{wdm} = 0.05$ keV and various fractions f_{wdm}

5.3 Analysis Results

To make sure that our analysis can be trusted we first run a ΛCDM scenario and compare it to the fiducial analysis made by the respective collaborations to gain confidence in our results. While perfect overlap is not necessary nor expected as the analysis choices and free-running parameters are different, there still needs to be a reasonable proximity in the two analysis. One can see from Fig.35 that the overlap in our implementation is very good compared with the full results from [Planck col. et al., 2020]. As expected from [Prince and Dunkley, 2019] the agreement is worst in the τ parameter despite the implementation of a gaussian-prior.

Regarding the analysis of the KiDS-1000 cosmic shear data the agreement is slightly less precise but still allows for high-confidence in our analysis results. The agreement is particularly strong on the A_{IA} parameter which shows that we used the same model modelling for Intrinsic Alignment as in [Asgari et al., 2021]. Our contours allow for slightly higher values of Ω_m (and therefore lower σ_8) but from the $\Omega_m - \sigma_8$ plot it is clear that the overlap of the "banana" shape is very good, which translates into excellent agreement in the S_8 parameter. The "thinner" appearance of our "banana" is likely due to the fixing of h and n_s to Planck18 values in our analysis and the omission of nuisance parameters the KiDS analysis included for redshift bin shifts.
Now that we are confident in our analysis we can include the mixed dark matter model and probe if any degeneracies appear.
From Fig.37 it appears clearly that the main cosmological parameters perfectly overlap, while only the σ_8 (and by correlation S_8) parameters go to lower values due to suppression of the linear matter power spectrum from the warm dark matter components allowed by the Planck only analysis. The lower values of σ_8 can be attributed to the small $m_w dm$ values as can clearly be seen in the $\log_{10}(1/m_{wdm}) - \sigma_8$ plot in Fig.37 from the downturn starting at $log_{10}(1/m_{wdm)} \sim 1 \longrightarrow m_{wdm} =$ 0.1keV.
We now turn our attention to the MDM analysis of the KiDS-1000 data presented in Fig.38. In this plot we observe an excellent superposition in all parameters between the ΛCDM and mixed dark Matter scenarios. As we will see in section 5.4 the constraints on the mixed dark matter are stronger in the KiDS-1000 analysis than in the Planck-18 TTTEEE analysis.

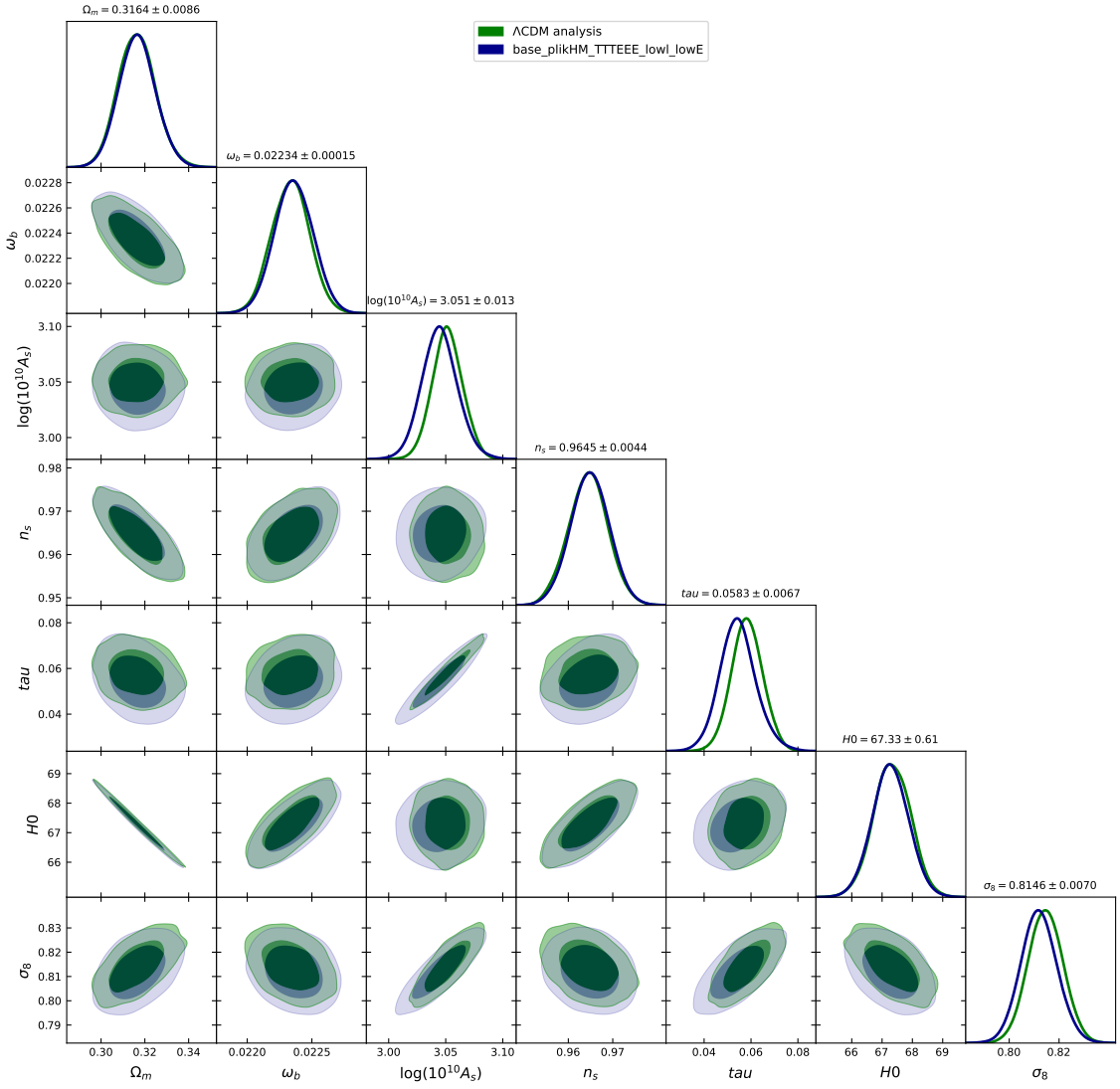

Figure 35: Our Monte-Carlo Markov Chain results compared to the fiducial analysis of the Planck18 of the TTTEEE-low ℓ spectra from [Planck col. et al., 2020]

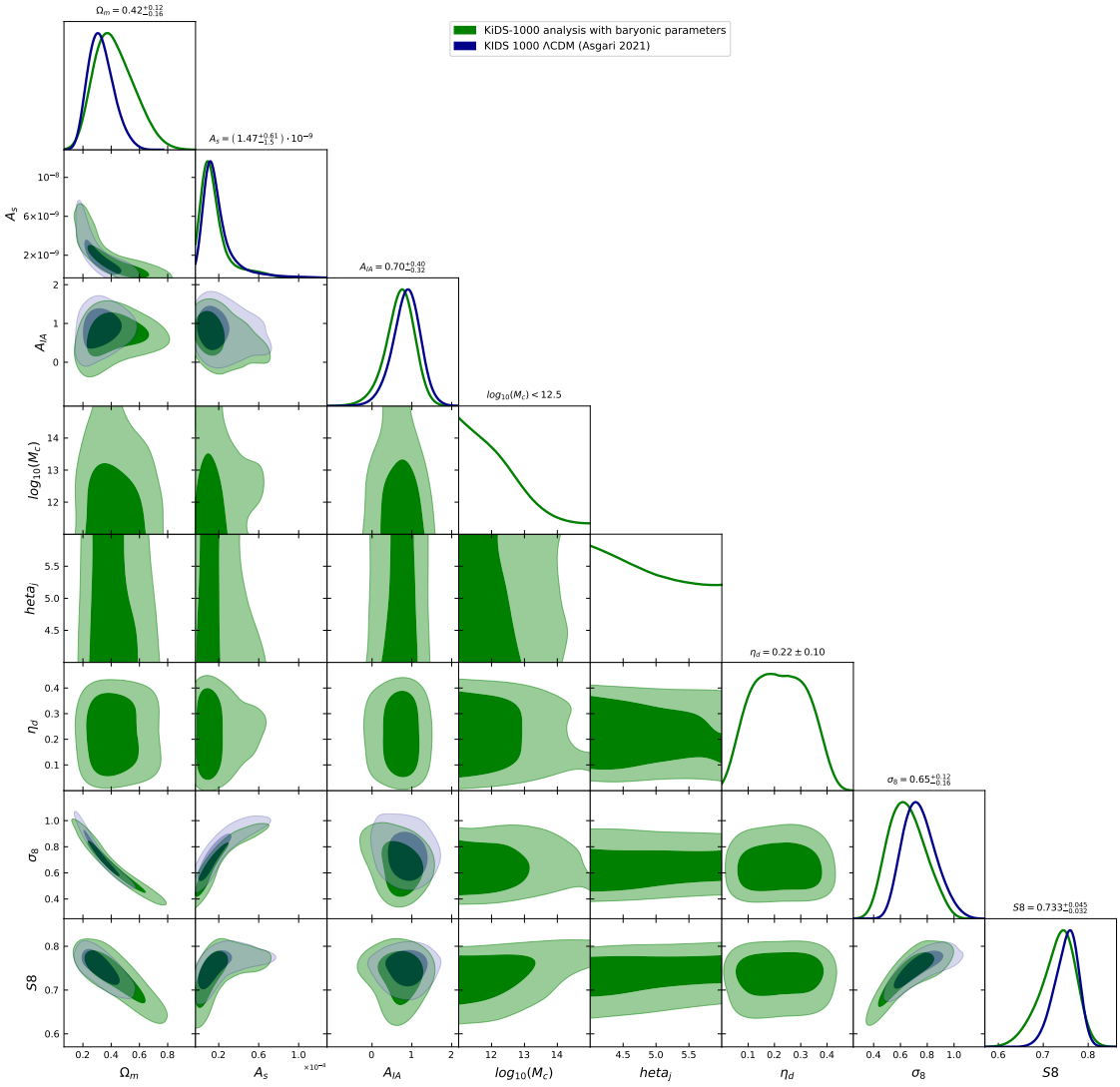

Figure 36: Our Monte-Carlo Markov Chain results compared to the fiducial analysis of the KiDS-1000 cosmic shear signal from [Asgari et al., 2021]

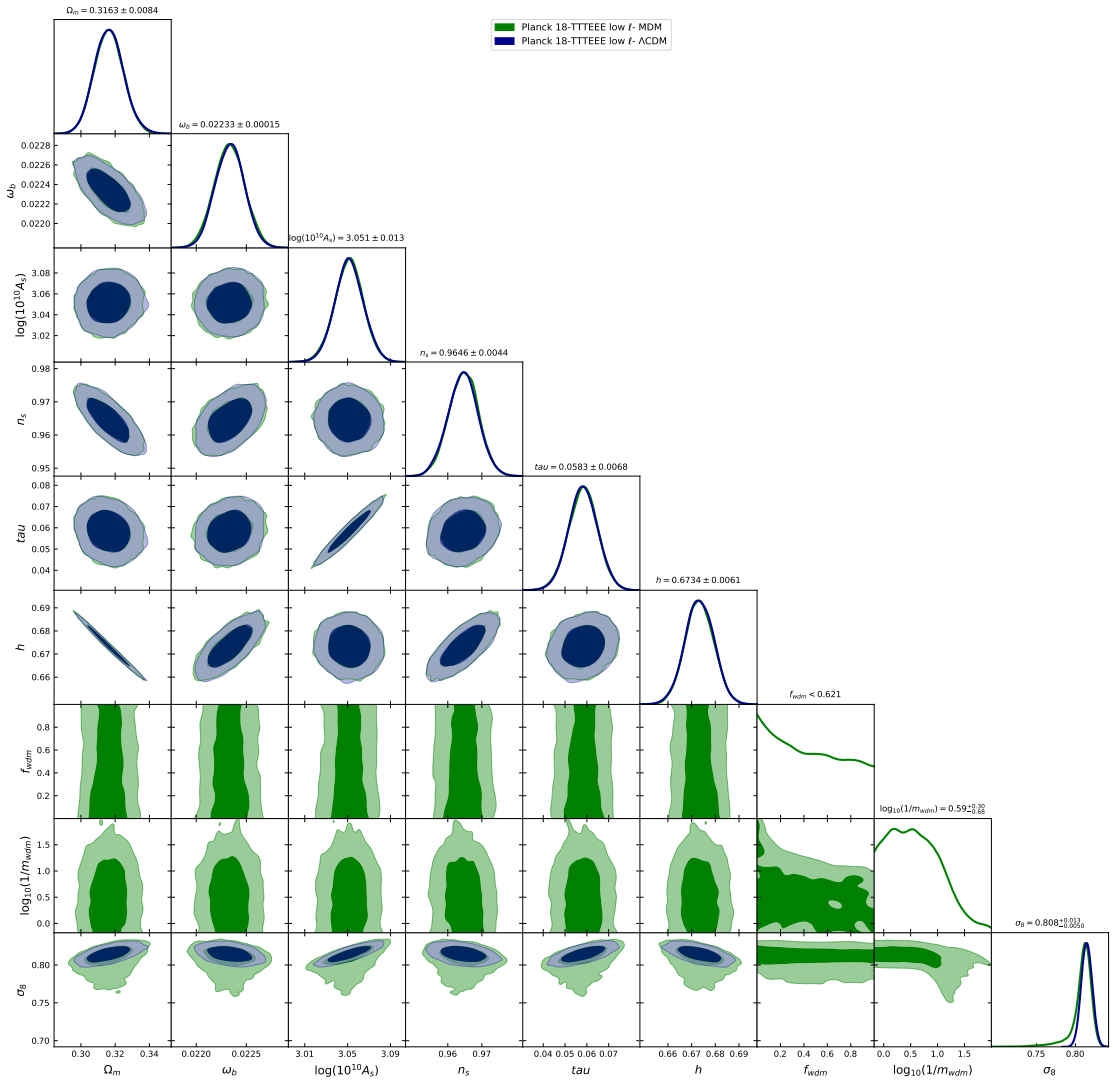

Figure 37: Our Monte-Carlo Markov Chain results comparing Planck-18 TTTEEE ΛCDM analysis in blue and ΛMDM analysis in green

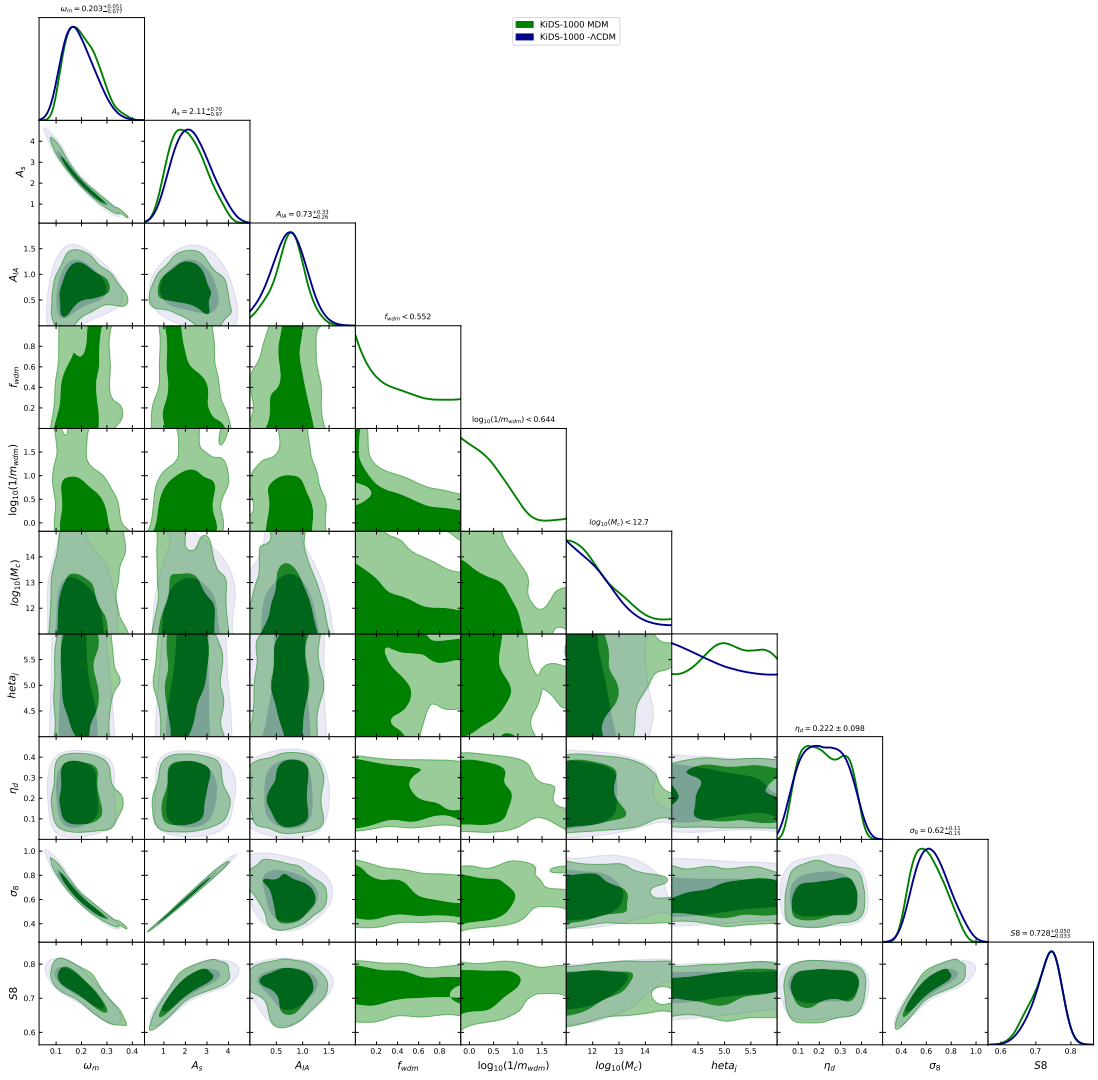

Figure 38: Our Monte-Carlo Markov Chain results of the KiDS-1000 cosmic shear signal comparing the MDM and ΛCDM scenarios

5.4 Mixed Dark Matter Constraints

The preferred region in the $[m_{wdm}, fwdm]$ plane are shown in Fig.39. For a pure WDM scenario (no cold dark matter, $f_{wdm} = 1$) the bayesian 95% confidence limit is $m_{wdm} > 0.095$keV for the Planck analysis and $m_{wdm} > 0.23$keV in the KiDS analyisis. In the sterile neutrino conversion this translates to $m_{nu_s} > 0.19$keV and $m_{wdm} > 0.59$keV respectively.
In the mixed dark matter scenario the idea is that along the $f_{wdm} = 0$ axes and for the highest thermal mass axes we tend to retrieve the ΛCDM scenario. When $f_{wdm} = 0$ this is trivial as the entirety of dark matter is cold. Regarding the mass, the higher it is, the smaller the free-streaming scale and therefore the smaller the suppression scale. While a 1.5keV mass particle still produces a suppression in the power spectrum, it does not appear at scales relevant for cosmic shear measurements and is therefore indistinguishable from a ΛCDM case in cosmic shear observations.
We can compare our limits to figure 8 in [Schneider et al., 2020]. A similar analysis to this work was carried out using baryonic parameters and the non-linear MDM corrections were included via the fitting function from [Kamada et al., 2016], which produces slightly stronger suppresions as shown in fig25. The analysis was carried out on a Euclid-type mock catalog and the constrains are therefore stronger due to the smaller error bars from the wider and more precise survey. The stated limit for a pure WDM cosmology for weak-lensing only measurements is $m_{wdm} > 300eV$ which is as expected better then the limit of this work $m_{wdm} > 230eV$. For $m_{wdm} = 30eV$ this work can exclude $f_{wdm} > 0.12$ while the forecast analysis can reject $f_{wdm} > 0.04$ for $m_{wdm} = 30eV$. This agreement shows both the consistency of our analysis and the importance of future surveys like Euclid to strengthen these bounds.
While it followed a very different analysis choice, our results can also be compared to [Das et al., 2021]. In this work an analysis was carried out using the Planck 18 TTTEEE spectrum, various BAO measurements, the growth function $f\sigma_8(z)$ of galaxy samples, the Pantheon SNIa catalogue and weak lensing measurements were included through a split-normal likelihood on S_8. The combination favored m_{sp}=27.49 eV and $\chi = 0.03$ corresponding to:

$$\omega_s = \frac{m_s}{94.05eV}\chi = \frac{27.49eV}{94.05eV}0.03 = 0.0087 \Longrightarrow f_{wdm} = \frac{\omega_{wdm}}{\omega_{dm}} = \frac{0.0087}{0.12} = 0.073 \tag{64}$$

where $\omega_{dm} = 0.12$ is the dark matter energy density from Planck18 constraint. This sterile neutrino mass therefore corresponds to $m_{thermal} = 11eV$ which is just at the limit of our analysis, and in conformity with the [Das et al., 2021] analysis disfavored by Planck 18 TTTEEE measurements alone. This combination value $f_{wdm} = 0.073, m_{wdm} = 11eV$ seems just disfavored at the 2σ limit in our KiDS-1000 analysis as can be read of in 39. It is nevertheless important to distinguish the two analysis as the parameters and prior ranges used for the modelisation are different. Our analysis allows for two degrees of freedom (energy density and mass) which retrieves the ΛCDM scenario in the high-mass/low f_{wdm} limit, while the analysis in [Das et al., 2021] varies $[\Delta N_{eff}, m_\nu]$ which has the consequence of putting the ΛCDM limit in the low-mass/low ΔN_{eff} limit.

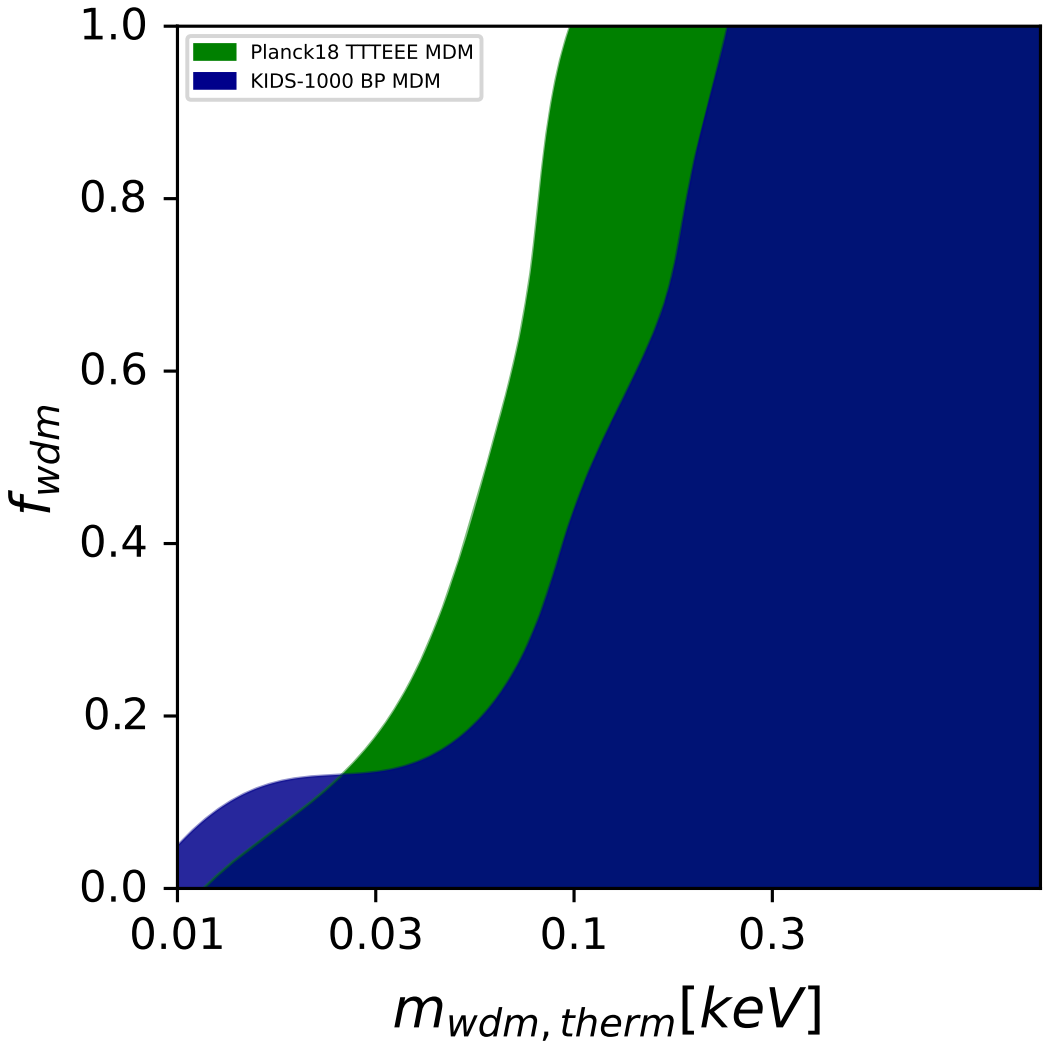

Figure 39: The constraints for the parameters m_{wdm} and f_{wdm} in the ΛMDM scenario

5.5 Impact on S_8 tension

The preferred region in the $[\Omega_m, S_8]$ plane are shown in Fig.39. We note that the tension between the ΛCDM contours in violet for Planck-18 and dark-blue of our KiDS-1000 ΛCDM analysis are in agreement with the contours shown in Fig.6 of [Asgari et al., 2021]. The MDM contours seem to be in slightly better agreement, mostly due to the lowering of the S_8 value in the Planck analysis. To evaluate the modification of the tension we use the tensionmeter module described in [Raveri and Doux, 2021]. In this estimation of the tension we do not account for the fact that using additional parameters might have the result of broadening the contours due to the new degrees of freedom.

To assess the tension between the contours we calculate the parameter shifts presented in Appendix B. This shift is given by $\Delta\theta = \theta_1 - \theta_2$ where θ are the driving parameters and the indices refer to the two sets to be compared. Once the parameter difference is obtained the probability of the shift

is assessed by:

$$\Delta = \int_{\mathcal{P}(\Delta\theta)>\mathcal{P}(0)} \mathcal{P}(\Delta\theta) d\Delta\theta \tag{65}$$

which is the posterior in dissacordance with the no-shift contour $\Delta\theta = 0$.
Using this methodology we find a shift of $\sigma_{\Lambda CDM}$=2.409 for the ΛCDM scenario and σ_{MDM}=1.855 for the mixed dark matter scenario.
To get an idea of the inclusion of Lyman-α measurements we select all points with $f_{wdm} < 0.2$ which are crudely allowed by Lyman-α measurements. With this scenario the probability in shift is $\sigma_{f_{wdm}<0.2}$ =2.052. This reduction in tension is interesting while not strongly significant but was obtained without the combined analysis of datasets.
For an interesting conceptual discussion of the combination of cosmological probes see [Massimi, 2021].

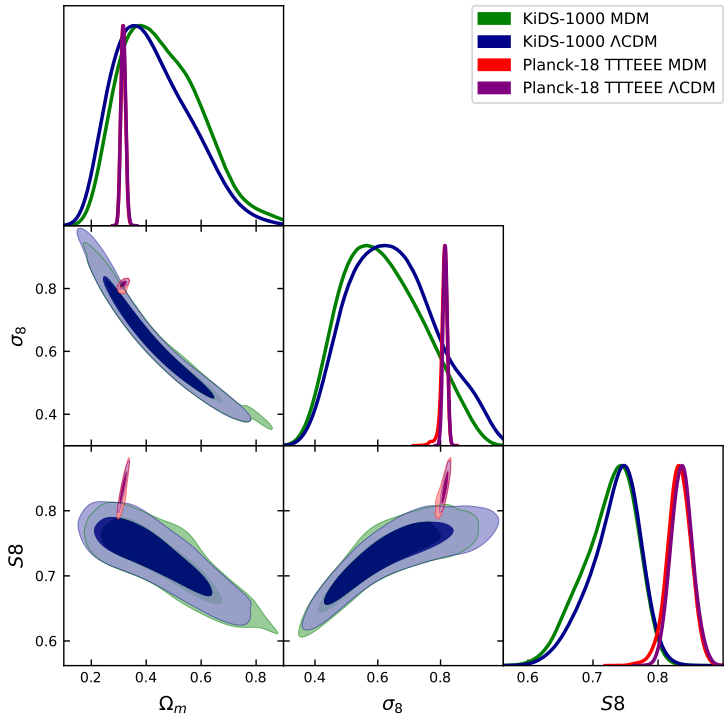

Figure 40: The constraints for the parameters S_8,σ_8 and Ω_m

6 Conclusion

In this work we probed the effects of a dark matter composed of a warm/hot part and a cold part on cosmic shear measurements and on the main Cosmic-Microwave Background observables. The concept of warm/hot matter is related to structure formation phenomenology and finds multiple particle physics candidates. We used the sterile neutrino formalism and derived constraints form the Planck 18 TTTEEE spectra. We also used a newly developed emulator to obtain the non-linear response from the mixed dark matter scenario, producing an accurate non-linear power spectrum we probed with the KiDS-1000 cosmic shear measurements. While not competitive with Lyman-α constraints, we derive an lower-limit $m_{wdm} > 95eV$ from Planck18 measurements and $m_{wdm} > 230eV$ from the analysis of the KiDS-1000 cosmic shear data. We find that no scenario with

$f_{wdm} < 0.1$ can be excluded, consistent with Lyman-α constraints.
We evaluated the impact of our analysis on the S_8-tension and found that it can alleviate the tension from 2.409σ to 1.855σ. This is due to the suppression in the linear power spectrum produced by low mass particles in the k-values $0.1 < k < 2h/\text{Mpc}$ which are selected by the top-hat in the σ_8 computation.
When excluding all points with $f_w dm \geq 0.2$, in lose accordance with Lyman-α measurements, the S_8-tension is of 2.052σ
In the future we hope that more advanced probes like the Euclid mission or LSST will be capable of improving these limits through more precise cosmic-shear measurements.

References

[Abdalla and Abellán, 2022] Abdalla, E. and Abellán, G. F. e. a. (2022). Cosmology Intertwined: A Review of the Particle Physics, Astrophysics, and Cosmology Associated with the Cosmological Tensions and Anomalies. *arXiv:2203.06142 [astro-ph, physics:hep-ph]*. arXiv: 2203.06142.

[Acero and Lesgourgues, 2009] Acero, M. A. and Lesgourgues, J. (2009). Cosmological constraints on a light nonthermal sterile neutrino. *Phys. Rev. D*, 79(4):045026.

[Aprile and Aalbers, 2018] Aprile, E. and Aalbers, J. e. a. (2018). Dark Matter Search Results from a One Tonne×Year Exposure of XENON1T. *Phys. Rev. Lett.*, 121(11):111302. arXiv: 1805.12562.

[Asgari et al., 2021] Asgari, M., Lin, C.-A., Joachimi, B., Giblin, B., Heymans, C., Hildebrandt, H., Kannawadi, A., Stölzner, B., Tröster, T., Busch, J. L. v. d., Wright, A. H., Bilicki, M., Blake, C., de Jong, J., Dvornik, A., Erben, T., Getman, F., Hoekstra, H., Köhlinger, F., Kuijken, K., Miller, L., Radovich, M., Schneider, P., Shan, H., and Valentijn, E. (2021). KiDS-1000 Cosmology: Cosmic shear constraints and comparison between two point statistics. *A&A*, 645:A104. arXiv: 2007.15633.

[ATLAS, 2021] ATLAS, c. (2021). Search for dark matter produced in association with a Standard Model Higgs boson decaying into b-quarks using the full Run 2 dataset from the ATLAS detector. *arXiv:2108.13391 [hep-ex]*. arXiv: 2108.13391.

[Bartelmann and Schneider, 2001] Bartelmann, M. and Schneider, P. (2001). Weak Gravitational Lensing. *Physics Reports*, 340(4-5):291–472. arXiv: astro-ph/9912508.

[Baur et al., 2017] Baur, J., Palanque-Delabrouille, N., Yèche, C., Boyarsky, A., Ruchayskiy, O., Armengaud, e., and Lesgourgues, J. (2017). Constraints from Ly-α forests on non-thermal dark matter including resonantly-produced sterile neutrinos. *J. Cosmol. Astropart. Phys.*, 2017(12):013–013. arXiv: 1706.03118.

[Bennett et al., 2021] Bennett, J. J., Buldgen, G., de Salas, P. F., Drewes, M., Gariazzo, S., Pastor, S., and Wong, Y. Y. Y. (2021). Towards a precision calculation of $N_{\rm eff}$ in the Standard Model II: Neutrino decoupling in the presence of flavour oscillations and finite-temperature QED. *arXiv:2012.02726 [astro-ph, physics:hep-ph]*. arXiv: 2012.02726.

[Bhattacharya et al., 2021] Bhattacharya, S., Das, S., Dutta, K., Gangopadhyay, M. R., Mahanta, R., and Maharana, A. (2021). Non-thermal Hot Dark Matter from Inflaton/Moduli Decay: The Momentum Distribution and Relaxing the Cosmological Mass Bound. *Phys. Rev. D*, 103(6):063503. arXiv: 2009.05987.

[Blumenthal et al., 1984] Blumenthal, G. R., Faber, S. M., Primack, J. R., and Rees, M. J. (1984). Formation of galaxies and large-scale structure with cold dark matter. *Nature*, 311(5986):517–525.

[Boyarsky et al., 2009] Boyarsky, A., Lesgourgues, J., Ruchayskiy, O., and Viel, M. (2009). Lyman-alpha constraints on warm and on warm-plus-cold dark matter models. *J. Cosmol. Astropart. Phys.*, 2009(05):012–012. arXiv: 0812.0010.

[Catelan et al., 2001] Catelan, P., Kamionkowski, M., and Blandford, R. D. (2001). Intrinsic and Extrinsic Galaxy Alignment. *Monthly Notices of the Royal Astronomical Society*, 320(1):L7–L13. arXiv: astro-ph/0005470.

[Das et al., 2021] Das, S., Maharana, A., Poulin, V., and Sharma, R. K. (2021). Non-thermal hot dark matter in light of the S_8 tension. *arXiv:2104.03329 [astro-ph]*. arXiv: 2104.03329.

[de Blok, 2010] de Blok, W. J. G. (2010). The Core-Cusp Problem. *Advances in Astronomy*, 2010:1–14. arXiv: 0910.3538.

[DES collab. et al., 2019] DES collab., c., Abbott, T. M. C., Abdalla, F. B., Avila, S., Banerji, M., Baxter, E., Bechtol, K., and et al., B. (2019). Dark Energy Survey Year 1 Results: Constraints on Extended Cosmological Models from Galaxy Clustering and Weak Lensing. *Phys. Rev. D*, 99(12):123505. arXiv: 1810.02499.

[Dodelson and Widrow, 1994] Dodelson, S. and Widrow, L. M. (1994). Sterile neutrinos as dark matter. *Phys. Rev. Lett.*, 72(1):17–20.

[Euclid col. et al., 2020] Euclid col., C., Knabenhans, M., Stadel, J., Potter, D., Dakin, J., Hannestad, S., Tram, T., Marelli, S., Schneider, A., and et al., T. (2020). Euclid preparation: IX. EuclidEmulator2 – Power spectrum emulation with massive neutrinos and self-consistent dark energy perturbations. *arXiv:2010.11288 [astro-ph]*. arXiv: 2010.11288.

[Fisher et al., 1999] Fisher, P., Kayser, B., and McFarland, K. S. (1999). Neutrino Mass and Oscillation. *Annu. Rev. Nucl. Part. Sci.*, 49(1):481–527. arXiv: hep-ph/9906244.

[Fixsen, 2009] Fixsen, D. J. (2009). The Temperature of the Cosmic Microwave Background. *ApJ*, 707(2):916–920. arXiv: 0911.1955.

[Foreman-Mackey et al., 2013] Foreman-Mackey, D., Hogg, D. W., Lang, D., and Goodman, J. (2013). emcee: The MCMC Hammer. *Publications of the Astronomical Society of the Pacific*, 125(925):306–312. arXiv: 1202.3665.

[Garzilli et al., 2021] Garzilli, A., Magalich, A., Ruchayskiy, O., and Boyarsky, A. (2021). How to constrain warm dark matter with the lyman-α forest. *Monthly Notices of the Royal Astronomical Society*, 502(2):2356–2363.

[Giblin et al., 2021] Giblin, B., Heymans, C., Asgari, M., Hildebrandt, H., Hoekstra, H., Joachimi, B., Kannawadi, A., Kuijken, K., Lin, C.-A., Miller, L., Tröster, T., Busch, J. L. v. d., Wright, A. H., Bilicki, M., Blake, C., de Jong, J., Dvornik, A., Erben, T., Getman, F., Napolitano, N. R., Schneider, P., and Shan, H. (2021). KiDS-1000 catalogue: Weak gravitational lensing shear measurements. *A&A*, 645:A105. arXiv: 2007.01845.

[Giri and Schneider, 2021] Giri, S. K. and Schneider, A. (2021). Emulation of baryonic effects on the matter power spectrum and constraints from galaxy cluster data. *J. Cosmol. Astropart. Phys.*, 2021(12):046. arXiv: 2108.08863.

[Hall, 2021] Hall, A. (2021). Cosmology from weak lensing alone and implications for the Hubble tension. *Monthly Notices of the Royal Astronomical Society*, 505(4):4935–4955. arXiv: 2104.12880.

[Henrot-Versillé et al., 2019] Henrot-Versillé, S., Couchot, F., Garrido, X., Imada, H., Louis, T., Tristram, M., and Vanneste, S. (2019). Comparison of results on $N_{\rm eff}$ from various *Planck* likelihoods. *A&A*, 623:A9.

[Heymans et al., 2021] Heymans, C., Tröster, T., Asgari, M., Blake, C., Hildebrandt, H., Joachimi, B., Kuijken, K., Lin, C.-A., Sánchez, A. G., Busch, J. L. v. d., Wright, A. H., Amon, A., Bilicki,

M., de Jong, J., Crocce, M., Dvornik, A., Erben, T., Fortuna, M. C., Getman, F., Giblin, B., Glazebrook, K., Hoekstra, H., Joudaki, S., Kannawadi, A., Köhlinger, F., Lidman, C., Miller, L., Napolitano, N. R., Parkinson, D., Schneider, P., Shan, H., Valentijn, E., Kleijn, G. V., and Wolf, C. (2021). KiDS-1000 Cosmology: Multi-probe weak gravitational lensing and spectroscopic galaxy clustering constraints. *A&A*, 646:A140. arXiv: 2007.15632.

[Hildebrandt et al., 2020] Hildebrandt, H., Köhlinger, F., Busch, J. L. v. d., Joachimi, B., Heymans, C., Kannawadi, A., Wright, A. H., Asgari, M., Blake, C., Hoekstra, H., Joudaki, S., Kuijken, K., Miller, L., Morrison, C. B., Tröster, T., Amon, A., Archidiacono, M., Brieden, S., Choi, A., de Jong, J. T. A., Erben, T., Giblin, B., Mead, A., Peacock, J. A., Radovich, M., Schneider, P., Sifón, C., and Tewes, M. (2020). KiDS+VIKING-450: Cosmic shear tomography with optical+infrared data. *A&A*, 633:A69. arXiv: 1812.06076.

[Hildebrandt et al., 2017] Hildebrandt, H., Viola, M., Heymans, C., Joudaki, S., Kuijken, K., Blake, C., Erben, T., Joachimi, B., Klaes, D., Miller, L., Morrison, C. B., Nakajima, R., Kleijn, G. V., Amon, A., Choi, A., Covone, G., de Jong, J. T. A., Dvornik, A., Conti, I. F., Grado, A., Harnois-Déraps, J., Herbonnet, R., Hoekstra, H., Köhlinger, F., McFarland, J., Mead, A., Merten, J., Napolitano, N., Peacock, J. A., Radovich, M., Schneider, P., Simon, P., Valentijn, E. A., Busch, J. L. v. d., van Uitert, E., and Van Waerbeke, L. (2017). KiDS-450: Cosmological parameter constraints from tomographic weak gravitational lensing. *Mon. Not. R. Astron. Soc.*, 465(2):1454–1498. arXiv: 1606.05338.

[Hirata and Seljak, 2010] Hirata, C. M. and Seljak, U. (2010). Intrinsic alignment-lensing interference as a contaminant of cosmic shear. *Phys. Rev. D*, 82(4):049901. arXiv: astro-ph/0406275.

[Jagvaral et al., 2022] Jagvaral, Y., Singh, S., and Mandelbaum, R. (2022). Intrinsic alignments of bulges and discs. *arXiv:2202.08849 [astro-ph]*. arXiv: 2202.08849.

[Joachimi et al., 2015] Joachimi, B., Cacciato, M., Kitching, T. D., Leonard, A., Mandelbaum, R., Schäfer, B. M., Sifón, C., Hoekstra, H., Kiessling, A., Kirk, D., and Rassat, A. (2015). Galaxy Alignments: An Overview. *Space Sci Rev*, 193(1-4):1–65.

[Joachimi et al., 2021] Joachimi, B., Lin, C.-A., Asgari, M., Tröster, T., Heymans, C., Hildebrandt, H., Köhlinger, F., Sánchez, A. G., Wright, A. H., Bilicki, M., Blake, C., Busch, J. L. v. d., Crocce, M., Dvornik, A., Erben, T., Getman, F., Giblin, B., Hoekstra, H., Kannawadi, A., Kuijken, K., Napolitano, N. R., Schneider, P., Scoccimarro, R., Sellentin, E., Shan, H. Y., von Wietersheim-Kramsta, M., and Zuntz, J. (2021). KiDS-1000 Methodology: Modelling and inference for joint weak gravitational lensing and spectroscopic galaxy clustering analysis. *A&A*, 646:A129. arXiv: 2007.01844.

[Kamada et al., 2016] Kamada, A., Inoue, K. T., and Takahashi, T. (2016). Constraints on mixed dark matter from anomalous strong lens systems. *Phys. Rev. D*, 94(2):023522. arXiv: 1604.01489.

[Kilbinger, 2015] Kilbinger, M. (2015). Cosmology with cosmic shear observations: a review. *Rep. Prog. Phys.*, 78(8):086901. arXiv: 1411.0115.

[Krause et al., 2016] Krause, E., Eifler, T., and Blazek, J. (2016). The impact of intrinsic alignment on current and future cosmic shear surveys. *Mon. Not. R. Astron. Soc.*, 456(1):207–222.

[Kuijken et al., 2019] Kuijken, K., Heymans, C., Dvornik, A., Hildebrandt, H., de Jong, J. T. A., Wright, A. H., Erben, T., Bilicki, M., Giblin, B., Shan, H.-Y., Getman, F., Grado, A., Hoekstra, H., Miller, L., Napolitano, N., Paolilo, M., Radovich, M., Schneider, P., Sutherland, W., Tewes,

M., Tortora, C., Valentijn, E. A., and Verdoes Kleijn, G. A. (2019). The fourth data release of the Kilo-Degree Survey: *ugri* imaging and nine-band optical-IR photometry over 1000 square degrees. *A&A*, 625:A2.

[Lesgourgues et al., 2013] Lesgourgues, J., Mangano, G., Miele, G., and Pastor, S. (2013). *Neutrino Cosmology*. Cambridge University Press.

[Lesgourgues and Tram, 2011a] Lesgourgues, J. and Tram, T. (2011a). The Cosmic Linear Anisotropy Solving System (CLASS) IV: Efficient implementation of non-cold relics. *J. Cosmol. Astropart. Phys.*, 2011(09):032–032. arXiv: 1104.2935.

[Lesgourgues and Tram, 2011b] Lesgourgues, J. and Tram, T. (2011b). The Cosmic Linear Anisotropy Solving System (CLASS) IV: efficient implementation of non-cold relics. *J. Cosmol. Astropart. Phys.*, 2011(09):032–032.

[Limber, 1953] Limber, D. N. (1953). The Analysis of Counts of the Extragalactic Nebulae in Terms of a Fluctuating Density Field. *ApJ*, 117:134.

[LSST collab., 2018] LSST collab., I. e. a. (2018). LSST: from Science Drivers to Reference Design and Anticipated Data Products. *arXiv:0805.2366 [astro-ph]*. arXiv: 0805.2366.

[Ma and Bertschinger, 1995] Ma, C.-P. and Bertschinger, E. (1995). Cosmological Perturbation Theory in the Synchronous and Conformal Newtonian Gauges. *ApJ*, 455:7. arXiv: astro-ph/9506072.

[Massimi, 2021] Massimi, M. (2021). Cosmic Bayes. Datasets and priors in the hunt for dark energy. *Euro Jnl Phil Sci*, 11(1):29.

[Mead et al., 2021] Mead, A., Brieden, S., Tröster, T., and Heymans, C. (2021). HMcode-2020: Improved modelling of non-linear cosmological power spectra with baryonic feedback. *Monthly Notices of the Royal Astronomical Society*, 502(1):1401–1422. arXiv: 2009.01858.

[Mead et al., 2016] Mead, A., Heymans, C., Lombriser, L., Peacock, J., Steele, O., and Winther, H. (2016). Accurate halo-model matter power spectra with dark energy, massive neutrinos and modified gravitational forces. *Mon. Not. R. Astron. Soc.*, 459(2):1468–1488. arXiv: 1602.02154.

[Moore et al., 1999] Moore, B., Ghigna, S., Governato, F., Lake, G., Quinn, T., Stadel, J., and Tozzi, P. (1999). Dark Matter Substructure in Galactic Halos. *The Astrophysical Journal*, 524(1):L19–L22. arXiv: astro-ph/9907411.

[Nadler et al., 2021] Nadler, E. O., Drlica-Wagner, A., Bechtol, K., Mau, S., Wechsler, R. H., Gluscevic, V., Boddy, K., Pace, A. B., Li, T. S., McNanna, M., Riley, A. H., García-Bellido, J., Mao, Y.-Y., Green, G., Burke, D. L., Peter, A., and Jain, B. e. a. (2021). Milky Way Satellite Census. III. Constraints on Dark Matter Properties from Observations of Milky Way Satellite Galaxies. *Phys. Rev. Lett.*, 126(9):091101. arXiv: 2008.00022.

[Niemi, 2011] Niemi, S.-M. (2011). Properties of galaxies and groups: Nature versus nurture.

[Nunes and Bonilla, 2018] Nunes, R. C. and Bonilla, A. (2018). Probing the properties of relic neutrinos using the cosmic microwave background, the Hubble Space Telescope and galaxy clusters. *Monthly Notices of the Royal Astronomical Society*, 473(4):4404–4409.

[Parimbelli et al., 2021] Parimbelli, G., Scelfo, G., Giri, S. K., Schneider, A., Archidiacono, M., Camera, S., and Viel, M. (2021). Mixed dark matter: matter power spectrum and halo mass function. *arXiv:2106.04588 [astro-ph]*. arXiv: 2106.04588.

[Planck col. et al., 2020] Planck col., C., Aghanim, N., Akrami, Y., Ashdown, M., Aumont, J., Baccigalupi, C., Ballardini, M., Banday, A. J., Barreiro, R. B., and Bartolo, N. e. a. (2020). Planck 2018 results. VI. Cosmological parameters. *A&A*, 641:A6. arXiv: 1807.06209.

[Potter et al., 2016] Potter, D., Stadel, J., and Teyssier, R. (2016). PKDGRAV3: Beyond Trillion Particle Cosmological Simulations for the Next Era of Galaxy Surveys. *arXiv:1609.08621 [astro-ph]*. arXiv: 1609.08621.

[Prince and Dunkley, 2019] Prince, H. and Dunkley, J. (2019). Data compression in cosmology: A compressed likelihood for Planck data. *Phys. Rev. D*, 100(8):083502. arXiv: 1909.05869.

[Raveri and Doux, 2021] Raveri, M. and Doux, C. (2021). Non-Gaussian estimates of tensions in cosmological parameters. *Phys. Rev. D*, 104(4):043504. arXiv: 2105.03324.

[Refregier et al., 2017] Refregier, A., Gamper, L., Amara, A., and Heisenberg, L. (2017). PyCosmo: An Integrated Cosmological Boltzmann Solver. *arXiv:1708.05177 [astro-ph]*. arXiv: 1708.05177.

[Sartoris et al., 2016] Sartoris, B., Biviano, A., Fedeli, C., Bartlett, J. G., Borgani, S., Costanzi, M., Giocoli, C., Moscardini, L., Weller, J., Ascaso, B., Bardelli, S., Maurogordato, S., and Viana, P. T. P. (2016). Next Generation Cosmology: Constraints from the Euclid Galaxy Cluster Survey. *Mon. Not. R. Astron. Soc.*, 459(2):1764–1780. arXiv: 1505.02165.

[Schneider, 2012] Schneider, A. (2012). Dark matter structures and the free streaming scale. Publisher: University of Zurich.

[Schneider, 2016] Schneider, A. (2016). Astrophysical constraints on resonantly produced sterile neutrino dark matter. *J. Cosmol. Astropart. Phys.*, 2016(04):059–059.

[Schneider et al., 2020] Schneider, A., Refregier, A., Grandis, S., Eckert, D., Stoira, N., Kacprzak, T., Knabenhans, M., Stadel, J., and Teyssier, R. (2020). Baryonic effects for weak lensing. Part II. Combination with X-ray data and extended cosmologies. *J. Cosmol. Astropart. Phys.*, 2020(04):020–020. arXiv: 1911.08494.

[Schneider and Teyssier, 2015] Schneider, A. and Teyssier, R. (2015). A new method to quantify the effects of baryons on the matter power spectrum. *J. Cosmol. Astropart. Phys.*, 2015(12):049–049. arXiv: 1510.06034.

[Takahashi et al., 2012] Takahashi, R., Sato, M., Nishimichi, T., Taruya, A., and Oguri, M. (2012). Revising the Halofit Model for the Nonlinear Matter Power Spectrum. *ApJ*, 761(2):152. arXiv: 1208.2701.

[Tarsitano et al., 2020] Tarsitano, F., Schmitt, U., Refregier, A., Fluri, J., Sgier, R., Nicola, A., Herbel, J., Amara, A., Kacprzak, T., and Heisenberg, L. (2020). Predicting Cosmological Observables with PyCosmo. *arXiv:2005.00543 [astro-ph]*. arXiv: 2005.00543.

[Tröster et al., 2021] Tröster, T., Asgari, M., Blake, C., Cataneo, M., Heymans, C., Hildebrandt, H., Joachimi, B., Lin, C.-A., Sánchez, A. G., Wright, A. H., Bilicki, M., Bose, B., Crocce, M., Dvornik, A., Erben, T., Giblin, B., Glazebrook, K., Hoekstra, H., Joudaki, S., Kannawadi, A.,

Köhlinger, F., Kuijken, K., Lidman, C., Lombriser, L., Mead, A., Parkinson, D., Shan, H., Wolf, C., and Xia, Q. (2021). KiDS-1000 Cosmology: constraints beyond flat ΛCDM. *A&A*, 649:A88. arXiv: 2010.16416.

[Van Waerbeke et al., 2013] Van Waerbeke, L., Benjamin, J., Erben, T., Heymans, C., Hildebrandt, H., Hoekstra, H., Kitching, T. D., Mellier, Y., Miller, L., Coupon, J., Harnois-Déraps, J., Fu, L., Hudson, M. J., Kilbinger, M., Kuijken, K., Rowe, B. T. P., Schrabback, T., Semboloni, E., Vafaei, S., van Uitert, E., and Velander, M. (2013). CFHTLenS: Mapping the Large Scale Structure with Gravitational Lensing. *Monthly Notices of the Royal Astronomical Society*, 433(4):3373–3388. arXiv: 1303.1806.

[Wright et al., 2020] Wright, A. H., Hildebrandt, H., van den Busch, J. L., and Heymans, C. (2020). Photometric redshift calibration with self-organising maps. , 637:A100.

A Appendix: The case of an additional massless component

In Section 2.7 we discussed the importance of N_{eff} and more precisely ΔN_{eff} to quantify an additional source of relativistic particles. While its impact on the linear perturbation theory is well understood, we wanted to test if its effects are well described by non-linear corrections to the power spectrum, as this is a parameter which is usually discarded when the emulators or fitting functions are calibrated. To test the good incorporation we ran N-Body simulations using the publicly available Pkdgrav3 [Potter et al., 2016] starting at z=49 with transfer functions computed with CLASS to test how the non-linear matter power spectrum reacts to a modification in N_{eff}. We ran different box sizes and number of particles to test the convergence of our simulations and to make sure that no finite-size effects were introduced by our box choice.
Once we retrieved the power spectrum of the simulation, we calculated the non-linear correction using different methods which are regularly used in the literature: [Mead et al., 2016], [Mead et al., 2021], [Takahashi et al., 2012], [Euclid col. et al., 2020] We plotted the corrections for $N_{eff} = 3.246$ and $N_{eff} = 3.446$. From figure Fig.41 we see that the non-linear prescriptions make a good job at capturing the change of N_{eff}.

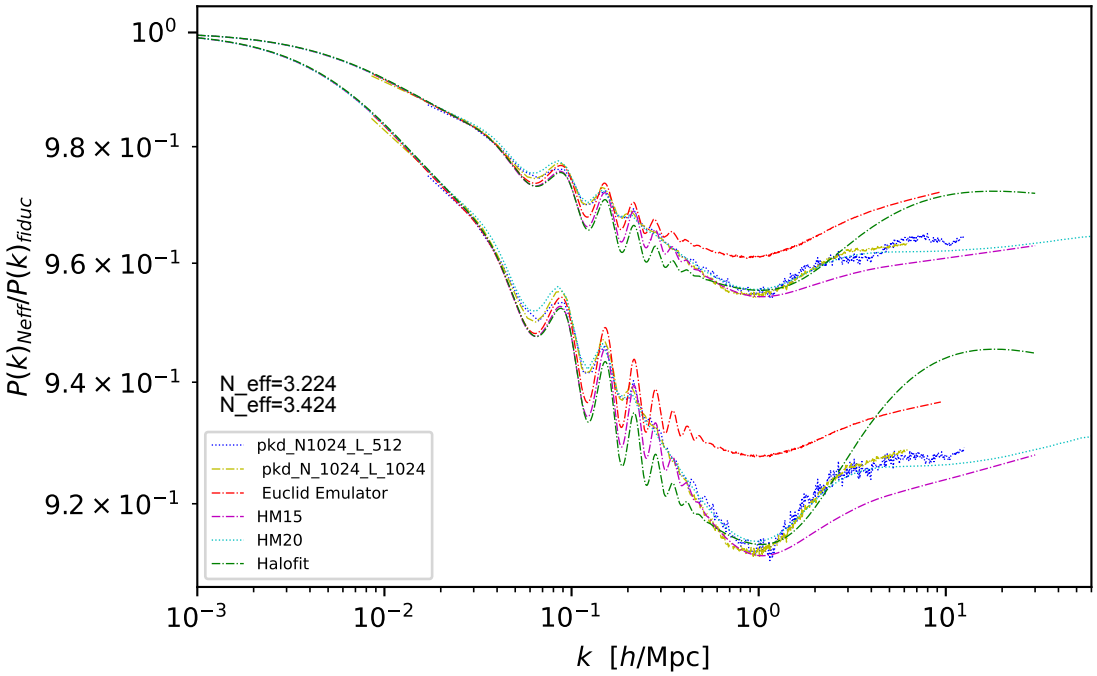

Figure 41: Comparison of non-linear prescriptions to capture ΔN_eff

To compute the transfer functions here we fixed ω_m, ω_b and h while varying N_{eff}. The difficulty as explained in [Lesgourgues et al., 2013] section 6.1.3, is that this has an effect on the redshift of equality between radiation and matter which Planck-18 estimated to it be $z_{eq} = 3411 \pm 48$. The relation between z_{eq} and N_{eff} is:

$$z_{eq} = \frac{\omega_m}{\omega_\gamma[1 + 0.2271 N_{eff}]} \tag{66}$$

or equivalently:

$$[1 + 0.2271 N_{eff}] = \frac{\omega_b(1 + \omega_b/\omega_c)}{z_{eq}\omega_\gamma} \tag{67}$$

with ω_γ and ω_c the photon and cold dark matter energy densities respectively.
When fixing the energy densities we get:

$$z_{eq} = 3410 \text{ for } N_{eff} = 3.046$$
$$z_{eq} = 3321 \text{ for } N_{eff} = 3.246$$
$$z_{eq} = 3236 \text{ for } N_{eff} = 3.446$$

while if we fix z_{eq} and ω_b/ω_c we can use a transformation:

$$(\omega_c, \omega_b, h) \longrightarrow ([\alpha\omega_c + (\alpha - 1)\omega_b], \omega_b, \sqrt{\alpha}h) \tag{68}$$

With $\alpha = [1 + 0.2271 N_{eff}]$. For our choice of parameters this gives the parameters:

$$h = 0.675,\ \omega_b = 0.0220,\ \omega_{cdm} = 0.1204 \text{ for } N_{eff} = 3.046$$
$$h = 0.684,\ \omega_b = 0.0220,\ \omega_{cdm} = 0.1242 \text{ for } N_{eff} = 3.246$$
$$h = 0.693\ ,\omega_b = 0.0220,\ \omega_{cdm} = 0.1280 \text{ for } N_{eff} = 3.446$$

On the Linear levels the resulting power spectra have very different appearances as can be seen in Fig.42, Fig.43, Fig.44 and Fig.45. We only calculated the non-linear response for the scenario in which z_{eq} varies and the other parameters are kept fixed.

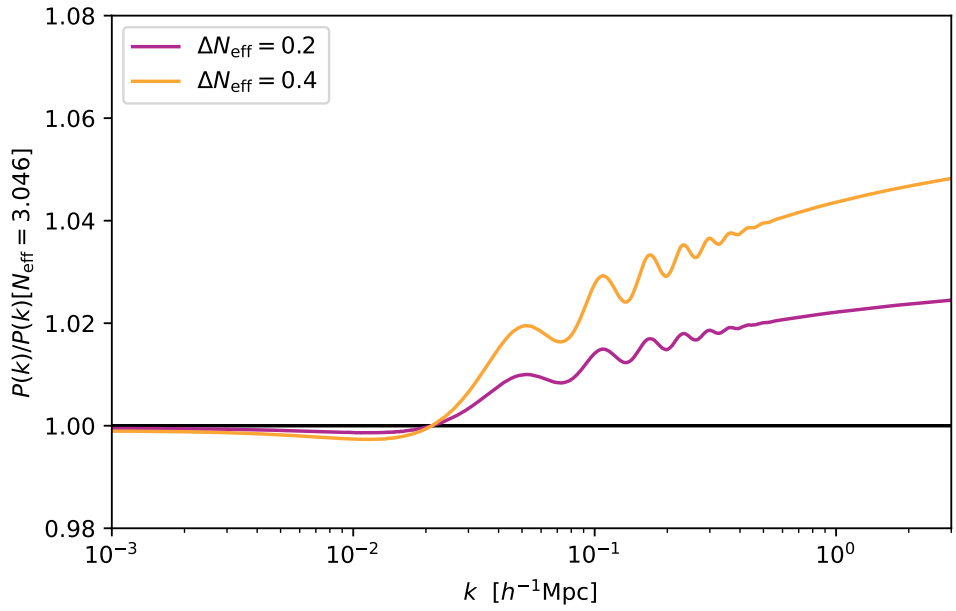

Figure 42: Ratio of matter power spectra for different ΔN_{eff}, with z_{eq} fixed and different ω_{cdm}

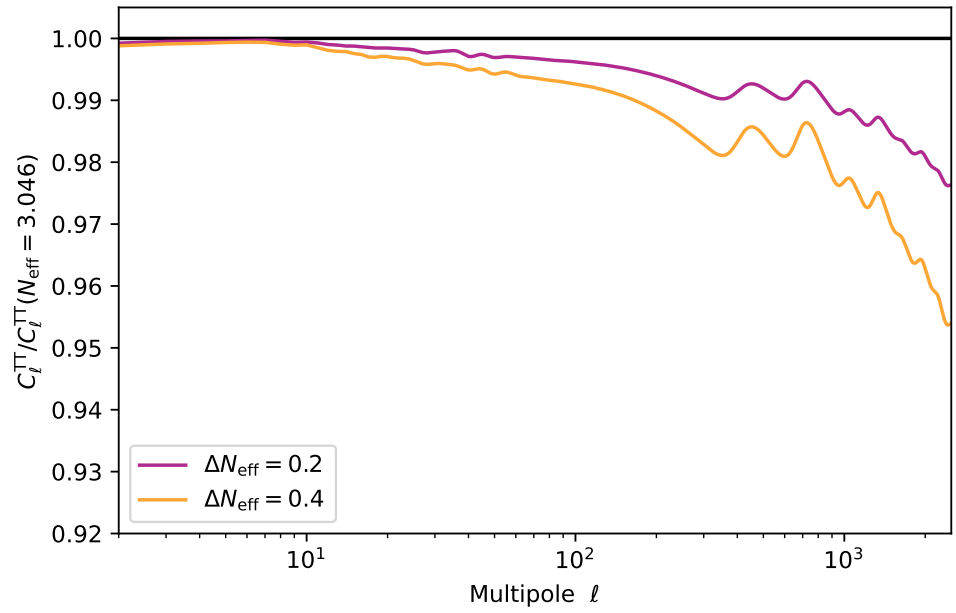

Figure 43: Angular power spectra for different ΔN_{eff}, with z_{eq} fixed and different ω_{cdm}

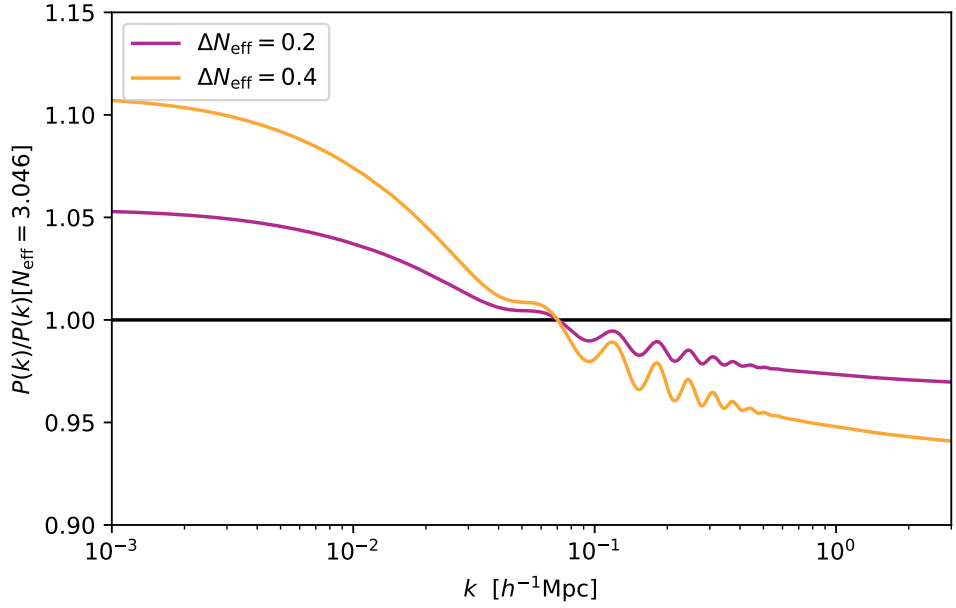

Figure 44: Ratio of matter power spectra for different ΔN_{eff}, with different z_{eq} and ω_{cdm} fixed

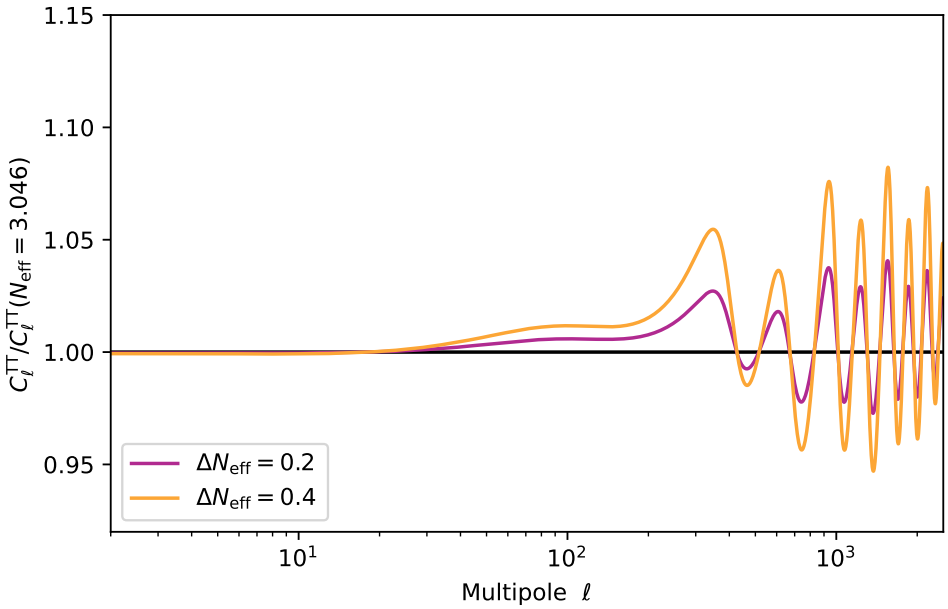

Figure 45: Angular power spectra for different ΔN_{eff}, with different z_{eq} and ω_{cdm} fixed

B Appendix: The parameter distances in Ω_m, σ_8, S_8

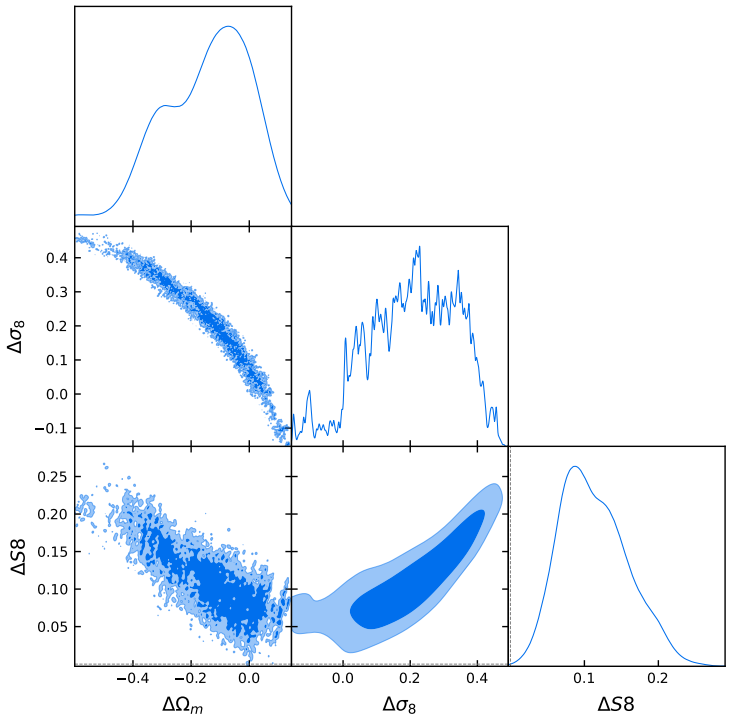

Figure 46: The parameter shift in ΛCDM

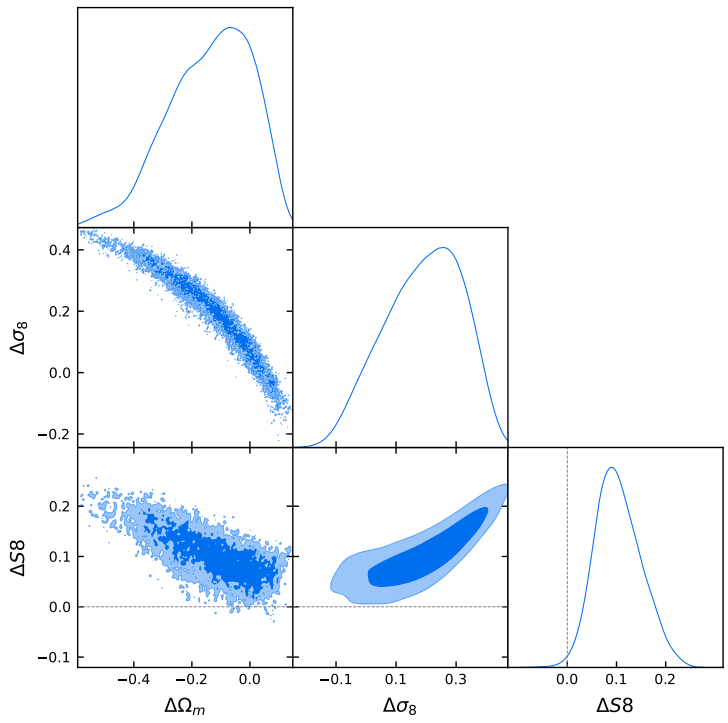

Figure 47: The parameter shift in MDM